P-93

A Study of Juncture Flow in the NASA Langley 0.3-Meter Transonic Cryogenic Tunnel

NASA Research Cooperative Agreement NCC1-98

Final Technical Report to the NASA Langley Research Center covering the period May 1990 - May 1992

Principal Investigator: Dr. Ndaona Chokani
Research Assistant: William E. Milholen II
Mechanical and Aerospace Engineering Department
North Carolina State University
Raleigh, NC 27695-7910

A Study of Juncture Flow in the NASA Langley 0.3–Meter Transonic Cryogenic Tunnel

Foreward

This report was prepared by North Carolina State University for the High–Reynolds–Number Aerodynamics Branch, Applied Aerodynamics Division, NASA Langley Research Center, Hampton, Virginia through Cooperative Agreement NCC1–98.

The authors are grateful to Pierce L. Lawing who served as program monitor, and who supported and encouraged all phases of the research program. Special thanks are extended to Veer N. Vatsa and Bruce W. Wedan for their many helpful discussions regarding the Navier–Stokes solver and grid generation code. The authors would also like to extend thanks to L. Elwood Putnam and Blair B. Gloss, and all other members of the High–Reynolds–Number Aerodynamics Branch, NASA Langley Research Center for their support.

This report concludes the work on Cooperative Agreement NCC1–98 which covered a period from May 1990 – May 1992.

Abstract

A numerical investigation of the interaction between a wind tunnel sidewall boundary layer and a thin low-aspect-ratio wing has been performed for transonic speeds and flight Reynolds numbers. A three-dimensional Navier-Stokes code was applied to calculate the flow fields. The first portion of the investigation examined the capability of the code to calculate the flow around the wing, with no sidewall boundary layer present. The second part of the research examined the effect of modeling the sidewall boundary layer. The results indicated that the sidewall boundary layer had a strong influence on the flow field around the wing. The viscous sidewall computations accurately predicted the leading edge suction peaks, and the strong adverse pressure gradients immediately downstream of the leading edge. This was in contrast to the consistent underpredictions of the free-air computations. The low momentum of the sidewall boundary layer resulted in higher pressures in the juncture region, which decreased the favorable spanwise pressure gradient. This significantly decreased the spanwise migration of the wing boundary layer. The computations indicated that the sidewall boundary layer remained attached for all cases examined. Weak vortices were predicted in both the upper and lower surface juncture regions. These vortices are believed to have been generated by lateral skewing of the streamlines in the approaching boundary layer.

Table of Contents

List of Symbols

b	wingspan, b = 16.52 cm
c	local chord length
C_f	local skin friction coefficient, $2\tau_w/(\rho_\infty U_\infty^2)$
C_p	surface static pressure coefficient, $(p - p_\infty)/q_\infty$
H	shape factor
i, j, k	grid index notation in the chordwise, normal, and spanwise directions
M	Mach number
P	static pressure
q	dynamic pressure
R	gas constant, in perfect gas relationship
Re	Reynolds number based on mean geometric chord
T	static temperature
u, v, w	normalized velocity components in the x,y,z directions
x, y, z	Cartesian coordinate system, with origin at the wing root leading edge
x/c	non dimensional chord fraction
2y/b	non dimensional semispan fraction
y^+	law of the wall coordinate, $u_\tau y/\nu$
α	angle of attack, deg.
δ	boundary layer thickness, mm
ν	kinematic viscosity
ρ	density
τ	local shear stress

Subscripts:

e	edge condition
w	wall value
∞	free stream value

1 Introduction

Juncture flows occur in many practical applications of interest to a fluid dynamics engineer. On aircraft, the juncture flow between the wing and fuselage is responsible for increased drag [1], and consequently increased fuel consumption. In wind tunnel testing, the juncture flow encountered on a sidewall mounted wing may significantly affect the quality of the data [2]. In contrast, juncture vortices may be helpful in combustion processes, where the mixing of the fuel and air mixture is improved. For example, Fig. 1 shows a schematic diagram of the juncture between a flat plate and a wing. In subsonic flow, the upstream influence of the wing causes the approaching streamlines to skew as the boundary layer prepares to flow around the wing. The approaching turbulent boundary layer separates upstream of the wing due to the large adverse pressure gradient imposed by the wing, and rolls up to form a horseshoe vortex in the juncture region [3]. The flow in the juncture region is characterized as a highly three-dimensional turbulent flow. Extensive experimental research has focused on juncture flow physics, and a few of these will be discussed here. Devenport et al. [4] have shown that the horseshoe vortex can dominate the juncture region, and trail downstream in the wake a considerable distance. They have also shown that the horseshoe vortex tends to be unsteady, further complicating the flow field.

Separation of the approaching boundary layer is not a necessary condition for the formation of juncture vortices. In situations where the boundary layer remains attached, the approaching streamlines are still skewed upstream of the wing as shown in Fig. 1. Shabaka and Bradshaw [3] have shown that lateral skewing of the streamlines in an approaching boundary layer is a powerful mechanism for the generation of juncture vortices.

One method commonly employed to reduce the adverse effects of the juncture flow involves the use of a fillet to provide a smooth transition from the fuselage or sidewall to the wing. Kubendran and Harvey [1] have shown that the addition of a leading edge fillet reduced drag in the juncture region, and improved the flow qualities in the downstream wake region. Scheiman and Kubendran [5] employed a fillet in the juncture region, and found that the fillet produced a more uniform flow field. These experiments have shown that simple modifications to the wing geometry can decrease the influence of the juncture flow.

Over the past decade, considerable progress has been made in the prediction of complex flows past modern aircraft using computational fluid dynamics (CFD) methods [6,7]. This progress is attributed to improved computational algorithms, more robust turbulence models, and the advent of supercomputers. The full Navier-Stokes equations can be numerically solved in an efficient and economical

manner for high Reynolds number flows, making CFD codes a viable tool for research and design. The pace of the introduction of CFD codes in aerodynamic design depends on their validation and their capability to support ground and flight experimental programs.

Several researchers have employed computational methods to model juncture flows. Shang [8] investigated the juncture interference between a wing and body at hypersonic Mach numbers. The computations agreed well with the experimental data, and showed improvements over previous inviscid results. Sung et al. [9] evaluated the performance of several juncture fillets in incompressible turbulent flow at moderate Reynolds numbers. Their results showed fair agreement with experimental data, and indicated that their computational method was capable of capturing important features of the juncture flow. Visbal [10] investigated the formation of a laminar horseshoe vortex system in a cylinder-plate juncture for incompressible flow. The computational results agreed well with experimental observations.

Several years ago, a program was initiated at NASA Langley Research Center to improve the design, construction, and testing techniques for thin, highly swept wing geometries. As part of this project, a thin, swept, low-aspect-ratio semi-span wing was constructed and tested in the 0.3-Meter Transonic Cryogenic Tunnel (TCT) , with an adaptive wall test section (AWTS). The wing was mounted on a sidewall turntable, and employed a juncture fillet. These tests were conducted over a wide range of Mach number and Reynolds number conditions, including flight Reynolds numbers, and resulted in a large experimental database [11]. The model was well instrumented with surface pressure taps, but there was still insufficient data to examine the highly three-dimensional flow field, especially in the juncture region and its' influence on the flow past the wing. This experiment is in contrast to those discussed above, in that it encompassed both compressible flow and high Reynolds numbers.

The adaptive wall technique minimizes blockage effects due to the model, and thus minimizes wall interference, ideally producing a free-air flow field around the wing. However, the adaptive wall technique does not compensate for the effects of the juncture flow inherent in sidewall testing. Thus, the purpose of this investigaion is to numerically model the interaction between the wind tunnel sidewall boundary layer, and the low-aspect-ratio wing. This will provide information about the characteristics of the juncture flow, and complement the existing experimental data. In order to meet this objective, a recently developed computational code for the solution of the three-dimensional compressible Reynolds averaged Navier-Stokes equations [12,13] was employed. The first portion of the research focuses on the capability of the computational code to calculate the flow field around the wing, with no sidewall boundary layer present. The second part of the investigation involves modifying the code to model the sidewall boundary layer. The computed wing pressure distributions are compared directly to the experimental data at

discrete spanwise locations. The solutions are analyzed in detail to determine the characteristics of the wing boundary layer, the sidewall boundary layer, and the juncture flow region. In addition, several parametric studies are presented which examine the influence of angle of attack, and freestream Mach number.

2 Numerical Procedure

2.1 Computational algorithm

The computational code, designated TLNS3D, developed at NASA Langley Research Center, for solving the time dependent, thin-layer Navier-Stokes (TLNS) equations for a body-fitted coordinate system was used in this study. Fuller details of the code are presented by Vatsa [12] and Vatsa and Wedan [13], but some salient features are discussed here. The conservation equations are discretized in a central differencing, finite volume formulation. An explicit multistage Runge-Kutta time stepping scheme, which is second order accurate, is used to advance the solution to steady-state. A non-isotropic dissipation model is employed to add controlled amounts of artificial dissipation to suppress oscillations which can occur in the vicinity of stagnation points and shock waves. This model scales the local value of artificial dissipation based on the local eigenvalue and the cell aspect ratio. Since the solutions of interest are steady state, the code takes advantage of four acceleration techniques: multigridding, local time stepping, three-dimensional residual smoothing, and enthalpy damping.

2.1.1 Governing equations

The unsteady, three-dimensional, Reynolds-averaged Navier-Stokes equations are written for a body fitted coordinate system in conservation law form as:

$$\frac{\partial(J^{-1}U)}{\partial t} + \frac{\partial F}{\partial \xi} + \frac{\partial G}{\partial \eta} + \frac{\partial H}{\partial \zeta} = \frac{\partial G_\nu}{\partial \eta} + \frac{\partial H_\nu}{\partial \zeta} \tag{2.1}$$

where t is time and J is the Jacobian of the coordinate transformation. The independent variables ξ, η, and ζ represent a body fitted coordinate system in the streamwise, normal, and spanwise directions respectively. The thin-layer assumption has been employed, and the only viscous diffusion terms retained are in the η and ζ directions. The vector U contains the conserved quantities: ρ, ρu, ρv, ρw, ρE. The vectors F, G, and H represent the inviscid fluxes, while G_ν and H_ν represent the viscous shear flux vectors. Reference [2] gives a full description of these vectors. As stated, Eqn. (2.1) represents the equation set solved for the case of modeling the viscous sidewall. The viscous shear flux in the η direction is due to the viscous

diffusion in the wing boundary layer, while the viscous shear flux in the ζ direction results from viscous diffusion in the sidewall boundary layer. For the case of the wing alone computations (free-air) , the last term in Eqn. (2.1) is dropped, since the only source of viscous diffusion is the wing boundary layer.

2.1.2 Boundary conditions

The four boundary conditions treated are: the wing surface; the far-field upstream boundary; the far-field downstream boundary (wake outflow): and the root plane of the wing. The treatment of the wing surface and the far-field downstream boundary, is identical for both the viscous sidewall case and the free-air case. The wing surface is treated as an adiabatic, no-slip surface, with the normal pressure gradient set to zero at the surface. The properties at the far-field downstream boundary are obtained using a zeroth-order extrapolation from the interior flow. For the free-air case, the two remaining boundary conditions are treated as follows. The far-field upstream boundary conditions are fixed using the Riemann invariants for a one-dimensional flow normal to the boundary. The root section of the wing is treated as a symmetry plane, where all flow conditions are treated as symnetric except the w component of velocity which is treated as antisymmetric, to ensure a no-flux, slip surface.

The two remaining boundary conditions for the viscous sidewall case are addressed here. The root section of the wing is treated as an adiabatic, no-slip surface , with the normal pressure gradient set to zero at the surface. This treatment is similar to the wing surface. The far-field upstream boundary is treated with a combination of inflow and outflow conditions, which are described in detail below.

Fig. 2 shows a schematic of the far-field upstream boundary, at the root plane of the wing. The determination of inflow or outflow along this boundary is found by examination of the sign of the dot product of the total velocity vector, and the outward facing normal for the given cell. For this example, inflow occurs between points a and b, where the dot product is negative. At point b, the flow is tangent to the boundary, and outflow occurs between points b and c, where the sign of the dot product is positive. Since the far-field upstream boundary extends a finite distance, it was necessary to impose an initial boundary layer thickness along the inflow portion, which would grow to the proper thickness in the vicinity of the wing. The characteristics of the wind tunnel sidewall boundary layer are presented in Reference [14]. The imposed boundary layer thickness is estimated by a turbulent flat plate power law, for incompressible flow [15] as:

$$\delta(x) = \frac{.37x}{(Re_x)^{1/5}} \tag{2.2}$$

where x is the physical coordinate in the chordwise direction, and Re_x is the local Reynolds number based on x.
The velocity profile within the boundary layer is given by the one-seventh power velocity law.
Since the approaching flow is compressible, the thermodynamic properties must also be specified within the imposed boundary layer. The static pressure is obtained from the interior flow using a zeroth-order extrapolation. The static temperature profile is given by the Crocco-Busemann relationship for an adiabatic flat plate [16] as:

$$T = T_e \left[1 + \frac{(\gamma - 1)}{2} M_e^2 \left\{ 1 - \left(\frac{u(x,z)}{U_e} \right)^2 \right\} \right] \tag{2.3}$$

where T_e is the freestream temperature, M_e the freestream Mach number, and $u(x,z)$ is the local velocity.
With the pressure and temperature known, the density is calculated using the perfect gas relationship.
Outside of the imposed boundary layer, the flow is treated as a uniform freestream. The static pressure is again extrapolated from the interior flow, while all other quantities are set to freestream values.
On the outflow portion of the boundary, the static pressure is specified as freestream. The remaining flow variables are obtained from zeroth-order extrapolations from the interior flow.

2.1.3 Turbulence modeling

Closure of the governing equations is accomplished with the equilibrium turbulence model of Baldwin-Lomax [17]. For the free-air computations, the eddy viscosity is calculated only for the wing boundary layer (which includes the wake). For the viscous sidewall modeling, an eddy viscosity distribution is calculated for both the wing boundary layer, and the sidewall boundary layer. In order to calculate the eddy viscosity in the juncture region, the two eddy viscosity distributions are combined using the blending function given in Reference [2]:

$$\overline{\varepsilon} = \frac{\varepsilon_w \ell_{sw}{}^2 + \varepsilon_{sw} \ell_w{}^2}{\ell_w{}^2 + \ell_{sw}{}^2} \tag{2.4}$$

where ε_w and ε_{sw} are the values of eddy viscosity from the wing and sidewall calculations respectively. The lengths, ℓ_w and ℓ_{sw}, are the respective normal distances from the wing and sidewall for a given point. At large distances from the juncture region, the blending function simplifies to give the appropriate eddy viscosity distribution for a single solid boundary. The sidewall boundary layer is

treated as fully turbulent, while outside this boundary layer on the wing surface, a fixed transition location was specified.

2.2 Experimental database

Extensive wind tunnel data was obtained for the model, and is described in detail by Chu and Lawing[11]. However, a brief summary of the experimental testing is presented.

Fig. 3 shows the dimensions of the semi-span wing model used for the experimental and computational study. The planform is similar to that of the canard on the X-29 experimental research aircraft. The wing cross-section is a NACA 64A-105, with a maximum thickness of 5% at 40% chord. The root section of the model was offset 1.25 cm from the tunnel sidewall by the use of a fillet, in order to minimize the influence of the juncture flow on the model.

The wing was tested in the NASA Langley 0.3-Meter Transonic Cryogenic Tunnel, which employs an adaptive wall test section (AWTS). Transition free testing was conducted over a wide range of tunnel conditions. The freestream Mach number was varied from 0.3 to 0.9, while the angle of attack was varied from -4° to 15°. The Reynolds number, based on the mean aerodynamic chord, was varied from 3.8×10^6 to greater than the flight Reynolds number. Chordwise surface pressure data were obtained at three spanwise locations: 2y/b = .391, .679, and .925. Since the data has yet to be released for general publication, the test Reynolds numbers used in this study will be referred to as low, medium, and high.

Fig. 4 shows a sketch of the adaptive wall test section. The entrance of the test section has a fixed geometry of 33cm × 33cm. The sidewalls are rigid, while the upper and lower walls are flexible, and moveable via computer controlled wall jacks. During a test, the pressure distributions are measured along the centerline of the top and bottom walls, along with the flexible wall positions. This data is input into a computer algorithm, which iteratively aligns the test section boundaries with the streamlines around the model, thus producing a flow field around the model which approaches free-air conditions. If the algorithm is successful, the walls are said to be streamlined. Murthy [18] has shown that the adaptive wall technique is an effective method for reducing wall interference effects in two-dimensional testing at moderate lift conditions. However, no previous studies have reported on the applicability of this technique for a low-aspect ratio wing, thus offering this computational study a unique opportunity to evaluate the adaptive wall strategy for three-dimensional testing, such as that discussed in Ref. [19].

2.3 Grid generation

An algebraic grid generation algorithm, based on the transfinite interpolation scheme developed by Eriksson [20], was used to generate three-dimensional grids of the C-O topology.
Fig. 5a shows a partial view of the grid used for the viscous sidewall modeling, while Fig. 5b shows a partial view of the grid used for the free-air computations. For clarity, not all grid lines are drawn. Grid points have been clustered to resolve the large gradients in the chordwise, spanwise, and normal directions. For the free-air computations, the upstream and downstream boundaries extended eight root chord lengths from the leading and trailing edges of the wing. The grid structure for the viscous sidewall modeling differs in many areas. To model the viscous sidewall, points have been clustered in the root region to resolve the sidewall boundary layer. The upstream boundary was located four root chord lengths from the wing leading edge, while the downstream boundary remained eight root chord lengths from the trailing edge. In contrast to the free-air grid, points were clustered at the upstream boundary for the viscous sidewall modeling, to avoid non-physical growth of the imposed sidewall boundary layer in this region.
The effect of moving the upstream boundary closer to the wing surface was examined by performing a free-air calculation on the smaller grid, with identical grid density and spacings. The test case chosen had a super-critical Mach number, and high wing loading. Both numerical results were compared, and it was found that the solutions were identical to plotting accuracy. For the sake of brevity, these results are not presented, but they indicate that reducing the extent of the upstream boundary should not introduce any numerical difficulties.
To accurately model the wing geometry, the grid was generated from coordinates measured directly off of the model. The only noted differences between the measured coordinates and those output from the grid generator were in the trailing edge and wing tip regions. The trailing edge on the model was blunt, while the grid generator has closed the trailing edge in order to have a single wake attachment point. The wing tip on the model was squared-off, while a rounded tip was used in the computations due to numerical considerations. In the early stages of the investigation, computations were performed on a grid generated from the theoretical coordinates of the wing, and compared to results obtained from the use of the measured coordinates. It was observed that there were negligible differences between the surface pressure distributions. From this comparison, it was considered that the use of the measured coordinates provided an accurate method for modeling the wing geometry.

3 Free-air computations

3.1 Grid refinement study

The following conditions of the high Reynolds number case, were used for the grid refinement study: $M_\infty = .70$, $\alpha = 8.23°$. Since no information was obtained in the experiment on the transition location, the effect of transition location was computationally studied. Several runs were conducted with transition locations ranging from 0.002c to 0.10c. The best agreement with the experimental data was obtained with a fixed-transition location at 2% chord; this location corresponded to the onset of the adverse pressure gradient at the inboard station. Due to the strength of the adverse pressure gradient, this would be the expected transition location.

The coarsest grid examined was 97×33×25 (chordwise, normal, and spanwise directions respectively), while the finest grid was 241×49×49. The convergence was examined by monitoring the residual error of the continuity equation as a function of the work unit, where the work unit represents the computational effort for one fine-mesh iteration. Fig. 6 shows the effect of the grid refinement on the convergence histories. Each case showed at least 5 orders of magnitude decrease in the log-residual. The finest grid required approximately 4 CPU hours on a Cray Y - MP supercomputer.

Fig. 7 compares the results of four representative grids. The effect of chordwise spacing is seen by comparing the 97×33×25 case with the 193×33×25 results. At the inboard section, the two solutions are nearly identical, showing only a slight underprediction of the suction peak; the agreement on the lower surface is excellent. At the two outer sections, the 193×33×25 case shows slight change over the 97×33×25 solution in terms of the suction peak prediction. A grid of 241×33×25 was also examined, but gave results very similar to the 193×33×25 grid, and is thus not presented here. Thus, 241 grid points in the chordwise direction were deemed adequate. The effect of normal spacing is seen by comparing the 193×33×25 case to the 241×49×25 results. The increase in normal spacing improved the modeling of the strong adverse pressure gradient, especially at the 92.5% span location. The normal grid density could not be increased further due to computer storage limits, thus 49 grid points were used in the subsequent computations. The final comparison is the effect of the spanwise density. The only small noticeable differences between the 241×49×25 and the 241×49×49 results occur at the outboard section.

The effects of grid refinement on the skin-friction distribution and velocity profiles were examined. Fig. 8a shows the influence of grid density on the C_f distribution

for the upper surface at the outboard section. Both the 97×33×25 and the 193×33×25 show the same trends. As before, the 241×33×25 case is not shown because it was similar to the 193×33×25 distribution. The effect of the increased resolution with 49 normal grid points can clearly be seen, with the appearance of a small separation zone.
The chordwise velocity profiles for the same section, at 0.50c are compared in Fig. 8b. Both the 97×33×25 and the 193×33×25 cases are similar, while the increase to 49 normal grid points showed a significant change in the character of the profile. Examining the spanwise velocity profiles, Fig. 8c, shows that grid density had a similar effect. At the two inboard sections, the two finest grids show identical results, while slight changes have occurred on the outer section. In both directions, the 241×49×49 grid again shows that the solution is grid independent. With the refined grid, the typical values of y^+ for the first grid point off of the surface were in the range of 1-5, with approximately 25 grid points clustered within the boundary layer. The finest grid of 241×49×49 was used in the subsequent computations. All cases presented in the following sections showed at least five orders of magnitude decrease in the log-residual, similar to those discussed above.

3.2 Influence of angle of attack-subcritical Mach number

The effect of angle of attack on the flow field was examined for a freestream Mach number of 0.70, and medium Reynolds number.

3.2.1 Influence of angle of attack on pressure distribution

Fig. 9 shows the computational results compared with the experimental data, for α = 3.17°. The agreement with the data is excellent. The suction peak at the leading edge is accurately predicted at the two outboard sections, while it is slightly underpredicted at the inboard section. The adverse pressure gradient downstream of the leading edge is well captured, as is the lower surface pressure distribution. The uneven C_p distributions observed in the computations were not related to the use of the measured coordinates, and are thought to be numerically generated. Fig. 10 shows the results obtained for α = 8.24°. The lower surface pressure distribution is accurately predicted, and the relatively flat portion of the last 60% of the upper surface is in good agreement with the data. However, at all three sections, the

adverse pressure gradient was not adequately captured. The final case, with $\alpha = 10.25°$, is shown in Fig. 11. The prediction of the magnitude of the leading edge suction peaks has improved, but the pressure recovery through the adverse pressure gradient is not well resolved. As with the previous cases, the lower surface pressure distribution is well modeled.
It is interesting to note that for each case that the suction peak level at each section was of the same order of magnitude. Because the wing leading edge is swept, this indicates that a favorable pressure gradient exists in the spanwise direction. This favorable pressure gradient will promote spanwise migration of the boundary layer, which will be examined in detail in another section.

3.2.2 Influence of angle of attack on computed skin-friction distribution

The computed skin-friction distributions for the upper surface of the wing are presented in Fig. 12. The first noticeable feature is the non-physical rise in the skin-friction at the trailing edge. This is due to the artificial dissipation scheme, as discussed by Swanson [21]. For the $\alpha = 3.17°$ case, the results predict the flow field to be completely attached. As α is increased, separation occurs at the two outboard sections, at the transition location. As the angle of attack is increased to 10.25°, the separated region has grown in both the spanwise and chordwise directions, following the expected trend. Further analysis of the computational results showed that the maximum height of the separated zone was less than 0.01c, and was thus not apparent from the pressure distributions.

3.2.3 Influence of angle of attack on the wing boundary layer

The influence of angle of attack on the development of the wing boundary layer was examined in detail from the computed shape factor distributions and velocity profiles. The shape factor distributions are shown in Fig. 13. All three sections show the characteristic increase in H in the developing laminar region, followed by an asymptotic decrease. At the two inboard sections, all three cases tend to approach the characteristic flat plate value of approximately 1.4. The large variations in H noted at the outboard section may be attributed to the separation present at the higher angles of attack. At the inboard section, the relatively large extent of nearly constant H values would suggest that the boundary layer profiles

are fairly similar for the three angles of attack. In contrast, the H distributions for the two outer sections would suggest that substantial changes in the boundary layer profiles can be anticipated.
These observations are verified by examining the chordwise velocity profiles at the 50% chord location, as shown in Fig. 14a. As α increases, the profiles become less full. Although the profiles are quite similar at the inboard section, the thinning of the profiles is more marked at the two outboard stations. The cause for this thinning can be deduced by examining the spanwise velocity profiles, shown in Fig. 14b. As the angle of attack is increased, the magnitude of the cross-flow increases, indicating a stronger spanwise migration of the boundary layer. This explains the less full chordwise profiles. It is significant to point out that end effects at the wing tip are evident in the existence of a second inflection point in the cross-flow profile at the outboard section.

3.2.4 Possible sources of discrepancies

From the above comparisons, it is evident that there were consistent differences between the computations and experimental data on the forward portion of the upper wing surface, as the angle of attack was increased. Several possible sources of this discrepancy were examined. The experimental pressure distributions suggest that a leading edge vortex develops on the inboard section of the wing, and is swept aft of the leading edge in the tip region. In depth examination of the computational results revealed that a leading edge vortical structure had not been predicted. Thus the Baldwin-Lomax turbulence model was modified to include the Degani-Schiff [22] modification, for the anticipated multiple vortex structure. No significant changes in the computations were obtained with this modification, but it should be noted that the rate of convergence was noticeably decreased. For these reasons, the original formulation of the turbulence model was employed for all the computations.
A second point of concern was the use of the two-dimensional wall adaption algorithm for the three-dimensional model. A comparison was made between the computed far-field pressures, and those obtained along the centerline of the AWTS flexible walls. Fig. 15 shows the comparison for the 8.24° case, for both the upper and lower walls. For reference, the leading edge of the fillet is at $x/c = 0.0$, and the trailing edge is located at $x/c = 1.0$. The results show good agreement upstream and downstream of the model, but diverge in the region of the wing. No experimental data were available off of the centerline for further comparison, but these results may indicate some limitations in the 2-D wall adaptation technique for the 3-D model testing.
Another possible source of discrepancy could be the pressure taps on the model. In the above discussion, it was noted that the computed flow field separated at the

outboard leading edge region as the angle of attack was increased. Under these conditions, the computations predicted that the attached laminar boundary layer thickness was of the same order as the pressure tap diameter. Taking this into consideration, the pressure taps would provide a disturbance to the boundary layer which was not modeled in the computations. Another point of consideration is the tendency of algebraic turbulence models to underpredict flow separation [23]. These two factors suggest that the computations may have underpredicted the extent of separation which may have occurred in the experiment.
Finally, the computations did not model the sidewall boundary layer. It is possible that the sharp leading edge of the fillet could cause the sidewall boundary layer to separate, and shed a vortex at higher angles of attack, and thus influence the pressure distribution on the wing surface. The lack of flow visualization data leaves this question unanswered, and underscores the importance of modeling the sidewall boundary layer.

3.3 Influence of angle of attack-supercritical Mach number

A second angle of attack sweep was conducted for a nominal freestream Mach number of 0.90, and medium Reynolds number. In contrast to the subcritical case, the experimental Mach number reported for each case presented here differed slightly. The difference in freestream Mach number is attributed to the adaptive wall strategy, which at supercritical Mach numbers tends to require larger corrections to the freestream Mach number. The actual freestream Mach number will be placed in parenthesis in the following discussion.

3.3.1 Influence of angle of attack on pressure distribution

Fig. 16 shows the computed surface pressure distribution at $\alpha = 5.46°$ ($M_\infty = 0.8860$). The agreement with the experimental data is quite good. The prediction of the lower surface pressure distribution is excellent. The location of the shock wave at the two inboard sections is exactly predicted. As with the subcritical Mach number results, the leading edge suction peak and subsequent adverse pressure gradient are not well resolved at all three sections. Fig. 17 examines the results as α is increased to $8.55°$ ($M_\infty = 0.8920$). The agreement on the lower surface at all sections, and the shock wave location at the inboard station is good. At the outboard section, the

shock wave location is less well predicted. Fig. 18 shows the solution for $\alpha = 10.31°$ ($M_\infty = 0.9073$). The prediction of the shock wave location at the inboard section is encouraging, as is the excellent modeling of the lower surface pressure distribution. As with the two previous cases, the leading edge suction peaks and adverse pressure gradients are not in good agreement with the data. The apparent lambda shock pattern observed in the data is not predicted by the computations.
Fig. 19 shows the computed upper surface pressure contours for the three angles of attack. The footprint of the normal shock wave is clearly evident for all three cases. As the angle of attack increases, the shock wave becomes stronger , and moves further aft on the wing. The predicted shock wave locations at the inboard section of the wing were predicted accurately for the three angles of attack, as discussed above. However, the actual shock strengths were over predicted as compared with the experimental data. The experimentally observed weaker shock waves are likely due to the interaction of the shock waves with the tunnel sidewall boundary layer [2]. The computed surface pressure contours show that the shock wave strengths are nearly constant over the inboard half of the wing up to the symmetry plane. A sidewall boundary layer would be expected to weaken the adverse pressure gradient through the shock wave. It is believed that by modeling the tunnel sidewall boundary layer, more accurate predictions of the flow field are possible.

3.3.2 Influence of angle of attack on computed skin-friction distribution

Fig. 20 shows the computed skin friction distributions for the upper surface of the wing for the three cases. As the flow decelerates through the shock wave, the skin-friction decreases as expected. In the regions upstream and downstream of the shock waves, the skin-friction decreases as α is increased. In all three cases, the predicted shock waves were not strong enough to induce flow separation. For two-dimensional flow, Liu and Squire [24] have shown that for various curved surfaces at transonic speeds, shock induced separation occurs when the peak Mach number ahead of the normal shock wave is about 1.33. For the 10.31° case, the peak Mach number ahead of the normal shock wave at the inboard section was approximately 1.30.

3.3.3 Influence of angle of attack on the wing boundary layer

The influence that the angle of attack has on the wing boundary layer was examined in detail from the shape factor distributions, velocity profiles, and surface streamline patterns. Fig. 21 shows the computed shape factor H plotted for the three cases. One feature that is common to all cases at the two inboard sections is the interaction of the shock wave. As the boundary layer passes through the shock wave interaction region, a strong adverse pressure gradient is experienced, which thins the profiles. As the profiles become less full, H increases. Further downstream, the profiles become fuller, and H recovers. Examining all three sections, the general trend is that H increases with angle of attack. The large jump in H at the outboard section at the two highest angles of attack is probably due to the trailing edge separation. Fig. 22a shows the chordwise velocity profiles at the 50% chord location. As with the subcritical cases discussed earlier, the profiles become less full as α is increased. This verifies the trends observed in the H distributions. At the two inboard sections, the profiles are quite similar at the two higher angles of attack. At the low angle of attack, a slight bulge in the profile is apparent at the second section. This may have been caused by the strong adverse pressure gradient imposed by the normal shock wave. An inflection point is present in the 8.55° case, at the outboard section. The inflection point moves toward the wing surface as x/c increases, and is responsible for the separation which occurs near the trailing edge. Fig. 22b shows the spanwise velocity profiles for the same location. As angle of attack increases, the magnitude of the cross-flow increases. As with the subcritical cases, the influence of the tip flow is apparent with the second inflection point present at the outboard section. For the 10.31° case, the character of the tip flow has changed drastically.
Fig. 23 shows surface streamline patterns for each case. Zero-mass particles were released one grid point above the wing surface along the leading edge, simulating the surface oilflow visualization technique. At $\alpha = 5.46°$, the streamlines are nearly parallel to the approaching freestream at the inboard portion of the wing. Moving outboard, the streamlines make a marked turn toward the tip, and begin to coalesce. At $\alpha = 8.55°$, the character of the streamline pattern has changed drastically. Outboard of the juncture fillet, the streamlines have coalesced into a structure which runs nearly parallel to the leading edge. It should be pointed out that this pattern does not represent the development of a leading edge vortex. This strong spanwise pattern is probably responsible for the inflection in the chordwise velocity profile, at the 50% chord location, as discussed above. At the outboard trailing edge, the streamlines turn nearly orthogonal to the freestream direction, where the flow has separated. When α is increased to 10.31°, the leading edge structure becomes stronger. The predominant flow direction in the tip region is in the spanwise direction. Even though experimental flow visualization data was not

available for comparison, the computations correctly predict that the spanwise migration of the boundary layer increases with angle of attack.

3.4 Influence of freestream Mach number

The influence of the freestream Mach number is examined from the $M_\infty = .70$, $\alpha = 10.25°$ and $M_\infty = .9073$, $\alpha = 10.31°$ cases.

Fig. 24 compares the pressure distribution for both cases. Most notable is that the pressure distribution for the higher Mach number is dominated by shock waves. The increased Mach number allows a large region of supersonic flow to develop, which is terminated by a normal shock wave. The lower surface distribution for both cases is similar, particularly in the leading edge region. At the two inboard sections, the level of the suction peak has decreased with the increase in Mach number.

Fig. 25 shows the influence of Mach number on the skin friction distribution. At the lower Mach number, at the inboard section there is a very dramatic rise in C_f at transition, followed by a monotonic decrease towards the trailing edge. At the two inboard sections, a separation zone is evident over the forward portion of the upper surface. In contrast at the higher Mach number, the skin friction rises more gradually downstream of transition. There is an expected decrease in skin friction across the shock wave as the flow is decelerated. Following this, the skin friction recovers towards the trailing edge.

Fig. 26 shows the effect of Mach number on the shape factor distribution. For the lower Mach number, the rapid variation at the transition location is attributed to the separated flow. At the two inboard locations, the higher Mach number varies monotonically from the transition location, to the shock wave interaction region. On the outboard section, the higher Mach number case shows that the profiles are continually thinning downstream of the transition location. Overall, the comparison shows that the profiles are fuller for the higher Mach number.

Fig. 27 compares the velocity profiles at 50% chord for the two cases. In the chordwise direction, the increase in Mach number has produced fuller profiles, as was indicated by the H distributions. In the spanwise direction, as the Mach number increases, the cross-flow has increased, while the character of the tip effects at the outboard section have changed significantly.

4 Viscous sidewall computations

4.1 Grid refinement study

The following conditions were chosen for the grid refinement study: $M_\infty = .70$, $\alpha = 8.24°$, Re = medium. The coarsest grid examined was $97\times49\times49$, while the finest was $241\times65\times49$. The far-field upstream boundary was originally located eight root chord lengths upstream of the leading edge. Preliminary computations indicated that the large aspect ratio cells at this boundary produced a non-physical growth of the sidewall boundary layer, in a zero pressure gradient region.

The cell spacing in the normal direction was based on a geometric progression. This provided clustering at the surface, to resolve the wing boundary layer, and progressively became coarser at the far-field upstream boundary. Due to the implementation of the transfinite interpolation scheme, the grid generator could not be modified to use a more suitable clustering function. For this reason, a short Fortran program was written that was capable of adding and clustering grid points at the upstream boundary. The resulting grid maintained the original grid distribution in the vicinity of the wing but modified the distribution in the farfield region.

Computations on a $97\times65\times49$ grid indicated that grid clustering at the upstream boundary removed the non-physical growth of the sidewall boundary layer. However, the sidewall boundary layer was observed to grow too rapidly in the interior portion of the grid, moving toward the wing surface. In this region, the grid cells were larger due to stretching of the grid. To decrease the stretching of the grid in the normal direction, the far-field upstream boundary was moved closer, such that it was four root chord lengths from the model. Results obtained with this grid indicated a more favorable growth rate for the sidewall boundary layer. The computations predicted a thicker sidewall boundary layer than given by Eqn. (2.2). Ref. [14] indicated that the sidewall boundary layer thickness was approximately 0.50in., at a location 1.8 root chord lengths upstream of the wing leading edge location. This measurement was made with an empty test section. The present computations predict a thickness of approximately 0.60in. at this location. The computations indicated that the pressure gradient was zero in this region, which justified the treatment of the upstream far-field boundary with flat plate assumptions. For purposes of comparison, a compressible flat plate boundary layer code, Anderson and Lewis [25], was employed to further examine the characteristics of the sidewall boundary layer. The thickness distribution predicted by this code was also thicker than that predicted by Eqn. (2.2), but only slightly thinner than

that predicted by TLNS3D, giving confidence in the Navier -Stokes computations. Based on the success of the free-air computations to accurately predict the locations of the normal shock waves on the upper wing surface at supercritical Mach numbers, the minimum number of chordwise grid points that could be used for the present computations was 241. This gave a minimum grid dimension of $241 \times 65 \times 49$. Even though clustering at the wing root was performed to resolve the sidewall boundary layer, the stretching of the grid in the near wall region produced large cells in the outer portion of the sidewall boundary layer, which may be responsible for the thicker boundary layer as discussed above. Due to computer memory and storage limitations, the spanwise grid could not be further refined, and to this extent future work should include further grid refinement.
Fig. 28 shows the convergence history for the $241 \times 65 \times 49$ grid. This computation required approximately 6 CPU hours on a Cray Y-MP supercomputer. The rate of convergence has decreased slightly, as compared to the free-air results (Fig. 6). With this grid, the typical values of y^+ for the first grid point off of the wing surface were again in the range of 1 - 5, with approximately 25 grid points clustered in the wing boundary layer. Typical y^+ values for the first grid point off of the viscous sidewall ranged from 1 - 10 in both the juncture region, and in the region of the far-field upstream boundary. In the remainder of the interior grid, the values ranged from 20 - 100, with approximately 15-20 points in the sidewall boundary layer. Again, this indicates the need for further studies.

4.2 Influence of sidewall boundary layer-subcritical Mach number

The first test case to examine the influence the sidewall boundary layer was: $M_\infty = .70$, $\alpha = 8.24°$, and Re = medium.

4.2.1 Influence of sidewall boundary layer on pressure distribution

Fig. 29 shows a comparison between the experimental pressure distribution and two computational results. The result obtained from the viscous sidewall modeling is denoted by VSW. while FA denotes the free-air computation. At the inboard station, the viscous sidewall computation shows a substantial improvement in the modeling of the strong adverse pressure gradient in the leading edge region, along

with improved prediction of the leading edge suction peak. At the middle section, slight improvements are noticed over the last 80% of the upper surface. Similar improvements are observed at the outboard station. The non-physical secondary suction peak is clearly evident at all three sections, and is attributed to poor grid resolution in this region. It is interesting to note that the lower surface pressure distribution is predicted equally well by both computations.
Fig. 30 compares the two computational results at two spanwise locations on the juncture fillet, where no experimental data was available. These locations are at the root and tip of the fillet. The results for the viscous sidewall modeling indicate that the upper surface experiences higher pressure, while the lower surface has not been significantly altered. The large uneven distributions observed at the second station are associated with the discontinuities in the slopes of the measured surface coordinates. Examination of the solution indicated that the sidewall boundary layer remained attached. Under such flow conditions, the low momentum of the sidewall boundary layer represents a locally decelerated flow field, as compared to free-air conditions. This accounts for the observed higher pressures on the inboard sections of the upper wing surface. This indicates that the presence of the sidewall boundary layer has reduced the favorable spanwise pressure gradient. The influence this has on the development of the wing boundary layer will be examined in detail below.

4.2.2 Influence of sidewall boundary layer on wing boundary layer

The influence of the sidewall boundary layer on the development of the upper surface wing boundary layer was examined in detail using the computed shape factor distributions, velocity profiles, and surface streamline patterns. Fig. 31 compares the shape factor distributions for the viscous sidewall computation directly to the free-air results. The larger values of H in the leading edge region are probably due to the larger separation. At all three stations, H decreases more rapidly in the adverse pressure gradient region in the leading edge region. This should be expected because the viscous sidewall computation showed improved modeling of the adverse pressure gradient. At the two inboard stations, both cases approach the flat plate value of approximately 1.1. For all three sections, the present computation has produced lower values of H over a large portion of the wing surface. This would tend to suggest that the chordwise velocity profiles have become fuller, and that the magnitude of the cross-flow has decreased.
Examination of both the chordwise and spanwise velocity profiles at the 50% chord location verifies these observations. The chordwise velocity profiles for both cases are shown in Fig. 32a. At all three locations, the viscous sidewall computation has predicted a fuller profile. At the inboard station the profiles are quite similar, while

larger differences are observed at the two outer stations. The mechanism responsible for the fuller profiles can be found by examining the spanwise profiles shown in Fig. 32b. At the two inboard sections, the present computation predicts that the magnitude of the cross-flow has decreased, while a slight increase is observed at the outboard station. The decreased spanwise migration of the boundary layer is responsible for the predicted fuller chordwise velocity profiles. At the inboard section, the peak spanwise velocity has been decreased by nearly 50%. The cause for the decreased cross-flow is the reduced favorable spanwise pressure gradient, generated by the sidewall boundary layer.

The decrease in the spanwise migration of the boundary layer is graphically illustrated in Fig. 33, which compares the surface streamlines for both cases. Particles have been released at similar locations for both cases. At the inboard portion of the wing, the viscous sidewall computation shows that the flow is predominantly in the streamwise direction. The streamlines adjacent to the wall appear to migrate toward the root section, then gradually move outward. This may be due to thinning of the sidewall boundary layer in this region, followed by its' growth as it travels downstream. This is in sharp contrast to the free-air computation which shows spanwise migration originating at the inboard portion of the wing. Both cases show the streamlines turning upstream in the leading edge region, where separation has occurred. In the tip region, both patterns are quite similar.

4.2.3 Characteristics of the juncture region

As mentioned above, the sidewall boundary layer remained attached for this test case. Several means which have been employed to investigate the flow physics of the juncture region include: total velocity contours at discrete chordwise locations, cross-flow velocity vector plots at the same locations, and surface streamline plots on the viscous sidewall.

The total velocity contours, normalized by the freestream velocity, will be presented at four spanwise locations on the wing. Fig. 34 shows these locations, looking in the upstream direction. At x/c = .25, thinning of the sidewall boundary layer is observed in the juncture region for the upper surface, while the boundary layer has become thicker on the lower surface. The thinning on the upper surface was due to flow acceleration around the leading edge of the fillet. Moving aft to x/c = .50, the sidewall boundary layer has become thicker and more uniform on both the upper and lower surfaces. This is consistent with the surface streamline pattern discussed above. Moving further aft, the boundary layer continues to grow thicker in both regions as expected. At the trailing edge, x/c = 1.0, the lower surface portion of the sidewall boundary layer is thicker.

Fig. 35 examines the cross-flow velocity vector plots in the juncture region at the same chordwise locations. At x/c = .25, a weak vortex is present in the juncture region of the lower surface. Below the vortex, the v velocity profile in the sidewall boundary layer is clearly shown and augments the vortical flow. It is interesting to note that large cross-flow velocities exist between the vortex center and the juncture surfaces. This indicates that the streamwise vorticity is maximum near the wall, and not at the vortex center. The increased flow toward the root section appears to be supplied by the inflow of the lower surface wing boundary layer. This implies that pressure gradient effects are responsible for the higher velocities, instead of lateral differences in the Reynolds stresses. The rotation direction of the vortex creates a downwash at the wall, which moves fluid away from the root section. Moving to the 50% chord location, a weak vortex has also appeared in the juncture region of the upper surface. The rotation direction is also counterclockwise, and has a stretched shape. This vortex moves fluid toward the root section. The lower vortex has moved away from the juncture, and toward the wall. At x/c = .75, the upper surface vortex has become stronger, and moved away from the wall. The lower surface vortex has become weaker, and has not changed position relative to the wing. This may have occurred due to the nearly constant streamwise pressure in this region. Finally at the trailing edge, both vortices have nearly vanished, and the dominant rotation observed results from the merging of the upper and lower surface wing boundary layers. Further examination of the flow field, one root chord length downstream of the trailing edge revealed that no vortices were present in the sidewall boundary layer. The regions in which the vortices were predicted tended to have fairly coarse grid spacing, indicating further grid refinement may be required to further resolve the behavior of the juncture vortices.

Fig. 36 compares streamline patterns for both cases at the root plane of the wing. The free-air computation predicts that the streamlines flow around the root section of the wing in a smooth manner. In contrast, the viscous sidewall computation predicts that the streamlines are skewed in the juncture region. Along the lower surface, the streamlines are displaced downward due to the downwash effect of the juncture vortex. Along the upper surface, both streamline patterns are similar over the first 25% of the chord. In this region, a juncture vortex was not predicted by the viscous sidewall computation. Over the last 75% of the chord, the streamlines have made a marked downward turn toward the surface. As discussed above, a juncture vortex was predicted in this region, with its' motion drawing fluid toward the wing surface.

Since the formation of the juncture vortices did not occur due to the separation of the sidewall boundary layer in the leading edge region, they are not termed as horseshoe vortices. Even though the approaching sidewall boundary layer did not separate, the approaching streamlines had to skew in order to flow around the leading edge of the wing. The leading edge of the fillet was highly swept, further adding to the three-dimensionality of the flow field. Lateral skewing of streamlines

in a boundary layer, such as in a wing-body juncture, has been shown to be a powerful mechanism for the generation of vortices in the juncture region [3]. This method of vortex generation does not require separation of the sidewall boundary layer. Thus, lateral skewing of the approaching streamlines is believed to be the primary cause for the generation of the juncture vortices.

4.3 Influence of sidewall boundary layer-supercritical Mach number, moderate wing loading

The second test case investigated had the following conditions: $M_\infty = 0.8860$, $\alpha = 5.46°$, Re = medium. No experimental data was available on the characteristics of the wind tunnel sidewall boundary layer for this Mach number. Since the imposed sidewall boundary layer thickness was only a function of the Reynolds number, the same thickness distribution was used as above.

4.3.1 Influence of sidewall boundary layer on pressure distribution

Fig. 37 shows the experimental pressure distribution compared to both computational results. At all three stations, the viscous sidewall computations is in excellent agreement with the data. The suction peaks in the leading edge region are well predicted, along with the strong adverse pressure gradient. Again, a slight secondary peak is observed near the transition location. At the two inboard stations, the presence of the sidewall boundary layer has reduced the predicted shock wave strength, as expected [2]. However, the predicted shock wave location has moved upstream slightly. This may indicate that the algebraic turbulence model has predicted a thicker wing boundary layer, which may be related to the blending function employed to obtain the eddy viscosity distribution. Downstream of the shock wave, the pressure recovery is again well modeled. Slight improvements are also observed on the lower surface pressure distribution at each station.
Fig. 38 examines the two computational results at the root and tip of the juncture fillet. Examination of the solution indicated that the sidewall boundary layer remained attached for this test case. The viscous sidewall computation predicted higher pressures over the upper surface, while the lower surface has not been significantly altered. At both sections, the sidewall boundary layer has substantially

reduced the shock wave strength. The higher pressure on the inboard portion of the wing indicates that the favorable spanwise pressure gradient has been reduced. Fig. 39 compares the upper surface pressure contours for the two computational results. The viscous sidewall computation clearly shows that the sidewall boundary layer has reduced the shock wave strength on the inboard portion of the wing. This is in contrast to the free-air result, where the predicted shock wave has a uniform strength in the root region. Also, the viscous sidewall computation predicts an oblique shock wave in the tip region, which merges with the normal shock wave. Examination of the solution indicated that the wing boundary layer remained attached.

4.3.2 Influence of sidewall boundary layer on the wing boundary layer

The influence that the sidewall boundary layer had on the upper surface wing boundary layer was examined using velocity profiles, and surface streamline patterns.

Fig. 40a compares the chordwise velocity profiles for both computations at the 50% chord location. At the inboard station, the viscous sidewall computation predicts a slightly fuller profile. At the middle station, the profile has become thinner. At the outboard station, the profile is slightly fuller, and quite similar to the profile at the inboard station. Examining the spanwise profiles, Fig. 40b, gives some insight into the observed chordwise profile changes. At the inboard station, the present computation again predicts an approximate 50% decrease in the peak spanwise velocity, with the external streamlines being less concave. The decreased spanwise migration of the wing boundary layer at this station is believed to be responsible for the fuller chordwise velocity profile. At the second station, the present computation predicts negligible cross-flow, which is in contrast to the free-air profile. At this station, the thinning of the chordwise profile was due to the improved modeling of the normal shock wave, and not due to increased cross-flow. At the outboard station, the peak cross- flow velocity has decreased slightly, while the influence of the tip vortex has changed. This would accounted for the observed fuller chordwise profile at this location.

The predicted surface streamline patterns for both cases are presented in Fig. 41. At the inboard portion of the wing, the viscous sidewall computation shows that the flow is predominantly in the streamwise direction. The inboard migration of the streamlines adjacent to the wall again suggests that the sidewall boundary layer is thinning in this region. The free-air streamline pattern shows that spanwise migration of the boundary layer originates in the root region. As discussed above, the sidewall boundary layer decreases the favorable spanwise pressure gradient, and

hence the spanwise migration of the wing boundary layer. The two patterns show some similarities in the tip region.

4.3.3 Characteristics of the juncture region

Fig. 42 shows the total velocity contours at four spanwise locations on the wing , again looking upstream. At x/c = .25, the sidewall boundary layer is observed to thin in the upper surface juncture region, while the lower portion is thicker and more uniform. The thinning is attributed to the favorable pressure gradient present in this region, and confirms the observed surface stream line pattern discussed above. Moving aft on the wing, the upper surface sidewall boundary layer becomes thicker and more uniform due to the adverse pressure gradient. The lower surface sidewall boundary layer grows at a slower rate, due to the nearly constant pressure in this region. At the trailing edge, the sidewall boundary layer has a fairly uniform thickness distribution.

Fig. 43 examines the cross-flow velocity vector plots at the same locations. At x/c = .25, a weak vortex is present in the lower juncture region. The rotational direction is again counterclockwise, and induces a downwash on the sidewall. The streamwise vorticity is again maximum near the solid surfaces, with the high velocities being supplied by the inflow of the lower surface wing boundary layer. Moving downstream to x/c = .50, a weak vortex has appeared in the upper juncture region. The rotation is also counterclockwise, and induces a downwash on the sidewall. The lower surface vortex has become weaker, and moved away from the juncture, toward the wall. At the 75% location, the upper vortex has moved upward and away from the wall, while the lower vortex has nearly disappeared. At the trailing edge, both vortices are weak, with the upper vortex still producing a downwash on the sidewall. Examination of the flow field one root chord length downstream of the trailing edge indicated that the upper surface vortex had disappeared. The lower surface vortex was much weaker, with only a negligible downwash induced on the sidewall.

The streamline patterns at the root of the wing are presented in Fig. 44. Again, the free-air case predicts that the streamlines flow around the root section in a smooth manner. The viscous sidewall computation predicts that the streamlines are skewed in the juncture region. The lower surface streamlines are again moved away from the juncture region by the downwash induced by the lower juncture vortex. Similarly, the upper surface streamlines are turned downward toward the juncture region by the downwash induced by the upper vortex.

As with the subcritical Mach number case, skewing of the streamlines in the approaching sidewall boundary layer at the leading edge of the wing is believed to be the mechanism responsible for the generation of the juncture vortices.

4.4 Influence of sidewall boundary layer-supercritical Mach number, high wing loading

The third test case investigated had the following conditions: $M_\infty = .9073$, $\alpha = 10.31°$, and Re = medium.

4.4.1 Influence of sidewall boundary layer on pressure distribution

Fig. 45 compares the experimental pressure distribution to both computations. The viscous sidewall computation shows vast improvements over the free-air result , and is in excellent agreement with the experimental data. At all stations, the leading edge suction peak is accurately predicted, again with a secondary peak present. An oblique shock wave has been predicted by the present computation. At the inboard section, the prediction of the oblique shock wave provides more accurate modeling of the strong adverse pressure gradient in the leading edge region. The experimental data suggests that a second, weaker oblique shock wave was present at approximately 20% chord. Even though the second oblique shock wave has not been resolved by the computation, the flow acceleration ahead of the normal shock wave is well predicted. The sidewall boundary layer has decreased the normal shock wave strength at the two inboard stations as expected, and agrees favorably with the data. As with the lower angle of attack case discussed above, the normal shock wave has moved slightly forward on the wing. Downstream of the shock wave, the pressure recovery is also modeled more accurately. At the outboard station, the oblique and normal shock waves have coalesced, with the wing boundary layer remaining attached. At all three stations, the viscous sidewall computation models the lower surface pressure distribution more accurately.

Fig. 46 compares the pressure distributions at the root and tip of the fillet for both cases. At the root section, the sidewall boundary layer has clearly decreased the shock wave strength, and spread its' associated adverse pressure rise over a larger region. The computation predicted that the sidewall boundary layer remained attached for this test case. The higher pressures on the inboard portion of the wing for the viscous sidewall case are attributed to the low momentum of the sidewall boundary layer. This indicates that the favorable spanwise pressure gradient has been decreased as with the two previous cases.

The computed upper surface pressure contours for both cases are presented in Fig.

47. The viscous sidewall computation clearly shows a lambda-shock wave pattern. The highly swept oblique shock wave merges with the normal shock wave in the tip region. At the inboard section of the wing, the normal shock wave is diffused by the sidewall boundary layer. This is in sharp contrast to the free-air result.

4.4.2 Influence of sidewall boundary layer on the wing boundary layer

Fig. 48a compares the predicted chordwise velocity profiles for both computations at the 50% chord location. At the inboard location, the profiles are nearly identical. At the middle section, the viscous sidewall computation exhibits a slightly thinner profile. The outboard section profiles are similar, except that an inflection point has not been predicted by the present computation. The spanwise velocity profiles are shown in Fig. 48b. At all three locations, the viscous sidewall computation has predicted a significant decrease in the spanwise migration of the wing boundary layer. This is attributed to the decreased favorable spanwise pressure gradient. Fig. 49 compares the surface streamline patterns for both cases. Over the inboard portion of the wing, the viscous sidewall computation predicts that the flow direction is predominantly in the streamwise direction. Over the outboard portion of the wing, the flow turns toward the root section in the leading edge region. The oblique shock wave then turns the flow towards the tip region. The normal shock wave has induced a small separation, at the midspan portion of the wing, as indicated by the S-shaped streamlines. The separation only extended approximately 2-4 grid points in the chordwise direction. The Mach number directly ahead of the shock wave was approximately 1.30. As with the previous cases, the free-air case exhibits a stronger cross-flow pattern, which again originates at the inboard section of the wing.

4.4.3 Characteristics of the juncture region

Fig. 50 shows the total velocity contours at four spanwise locations on the wing. At x/c=.25, the sidewall boundary layer has become thinner in the upper surface juncture region, while thickening is observed in the lower surface juncture region. Moving aft to x/c=.50, the sidewall boundary layer in the upper juncture region has become thinner, while the lower portion has become slightly thicker. The thinning observed in the upper juncture region is attributed to the flow acceleration ahead of the normal shock wave. Moving further aft, the upper portion of the sidewall

boundary layer continues to thicken, until at the trailing edge both portions have similar thickness distributions. As before, the slower growth of the sidewall boundary layer in the lower juncture region is attributed to the nearly constant pressure in this region.

Fig. 51 examines the cross-flow velocity vectors for the same locations. At x/c=.25, a weak vortex is again predicted in the lower surface juncture region. Large velocities are again observed between the vortex center and the solid surfaces. The inflow of the lower surface wing boundary layer supplies the increased flow toward the sidewall. At x/c= .50, a vortex has been predicted in the upper surface juncture region, with the center of circulation above the juncture and close to the wall. The lower juncture vortex has become larger, and moved downward away from the wing. At x/c=.75, the upper juncture vortex has become larger and moved away from the wall toward the wing, inducing a stronger downwash on the sidewall. The lower juncture vortex has become weaker and moved closer to the wing. Finally, at the trailing edge, both vortices have become weaker. Further probing of the solution revealed that no vortices were present in the sidewall boundary layer one root chord length downstream of the trailing edge.

Fig. 52 compares the streamline patterns at the root of the wing for both computations. Again, the viscous sidewall computation shows how the streamlines have been skewed by the juncture vortices. As with the two previous cases, skewing of the streamlines in the approaching sidewall boundary layer is believed to be responsible for the formation of the juncture vortices.

5 Conclusions

A numerical investigation of the interaction between a wind tunnel sidewall boundary layer and a thin low-aspect-ratio wing has been performed for transonic speeds and flight Reynolds numbers. A recently developed, state-of-the-art computational code for the solution of the three-dimensional compressible Reynolds averaged Navier-Stokes equations was modified to model the sidewall boundary layer. The computed surface pressure distributions were compared directly to experimental data. In addition, the computed solutions were analyzed to determine the characteristics of the wing boundary layer, the sidewall boundary layer, and the juncture flow region. The results which can be drawn from this investigation are:

1. The viscous sidewall computations accurately predicted the leading edge suction peaks for all test cases examined. The strong adverse pressure gradients directly downstream of the leading edge were also well modeled. This is in contrast to the free-air computations, which consistently underpredicted the leading edge suction peaks, and poorly predicted their associated adverse pressure gradients. Both computations accurately modeled the lower surface pressure distribution, with the viscous sidewall computations showing slight improvements.
2. For the super-critical Mach number cases, the viscous sidewall computations accurately predicted the normal shock wave strengths on the inboard portion of the wing. The low momentum of the sidewall boundary layer diffused the pressure rise associated with the shock waves as expected. The free-air computations overpredicted the shock wave strengths in this region.
3. The viscous sidewall computations indicated that the presence of the sidewall boundary layer significantly decreased the spanwise migration of the wing boundary layer flow. The viscous sidewall computation predicted higher pressures in the juncture region, due to the low momentum of the sidewall boundary layer. These higher pressures decreased the favorable spanwise pressure gradient, and thus decreased the cross-flow.
4. The viscous sidewall computations predicted that the sidewall boundary layer remained attached for all test cases analyzed. The upper portion of the sidewall boundary layer was observed to thin in the leading edge region due to the favorable pressure gradient, and became thicker and more uniform toward the trailing edge. The lower portion was observed to grow at a slower rate, due to the large region of nearly constant pressure, and had a fairly uniform thickness distribution. At the trailing edge, the upper and lower portions had similar thickness distributions. These trends were observed for all test cases.

5. Weak juncture vortices were predicted in both the upper and lower juncture regions for all test cases. Lateral skewing of the streamlines in the approaching sidewall boundary layer is believed to be the primary vortex generation mechanism. The circulation of the vortices created a downwash on the sidewall, which skewed the surface streamlines in the root region. This is in sharp contrast to the smooth streamline patterns predicted by the free-air computations.

6 Acknowledgements

This research was supported by NASA Research Cooperative Agreement NCC1-98.

7 Publications

1. Milholen, W. E., Chokani, N., Lawing, P. L. and Chu, J., "Evaluation of a Three–Dimensional Navier–Stokes Solver for Transonic Flow Over a Low Aspect Ratio Wing Mounted in a Wind Tunnel," AIAA 91–1725, AIAA 22^{nd} Fluid Dynamics, Plasma Dynamics and Lasers Conference, Honolulu, Hawaii, June 24–26, 1991.

2. Milholen, W. E. "Numerical Modeling of Transonic Juncture Flow," *MS Dissertation*, Mechanical and Aerospace Engineering Department, North Carolina State University, Raleigh NC, June 1992.

3. Milholen, W. E. and Chokani, N., "Numerical Modeling of Transonic Juncture Flow," AIAA 92–4036, AIAA 17^{th} Aerospace Ground Test Conference, July 6–8, 1992, Nashville, Tennessee.

8 References

1. Kubendran, L.R. and Harvey, W.D., *"Juncture Flow Control Using Leading-Edge Fillets,"* AIAA Paper 85-4097, October 1985.

2. Vatsa, V.N. and Wedan, B.W., *"Navier-Stokes Solutions For Transonic Flow Over A Wing Mounted In A Tunnel,"* AIAA Paper 88-0102, January 1988.

3. Shabaka, I.M.M.A. and Bradshaw, P., *"Turbulent Flow Measurements in an Idealized Wing/Body Junction,"* AIAA Journal, Vol. 19, February 1981, pp. 131-132.

4. Devenport, W.J., Agarwal, N.K., Dewitz, M.B., Simpson, R.L., and Poddar, K., *"Effects of a Fillet on the Flow Past a Wing-Body Junction,"* AIAA Journal, Vol. 28, December 1990, pp. 2017-2024.

5. Scheiman, J. and Kubendran, L.R., *"Laser Velocimeter Measurements in a Wing-Fuselage Type Juncture,"* NASA TM-100588, April 1988.

6. Marvin, J. G. and Holst, T. L.,*"CFD Validation for Aerodynamic flows - Challenge for the '90's,"* AIAA Paper 90-2995CP, August 1990.

7. Yeh, D.T., George, M.W., Clever, W.C., Tam, C.K., and Woan, C.J., *"Numerical Study of the X-31 High Angle-of-Attack Flow Characteristics,"* AIAA Paper 91-1630, June 1991.

8. Shang, J.S., *"Numerical Simulation of Wing-Fuselage Interference,"* AIAA Journal, Vol. 20, December 1982, pp. 1657-1658.

9. Sung, Chao-Ho, Griffin, M.J., and Coleman, R.M., *"Numerical Evaluation of Vortex Flow Control Devices,"* AIAA Paper 91-1825, June 1991.

10. Visbal, M.R., *"The Laminar Horseshoe Vortex System Formed at a Cylinder/Plate Juncture,"* AIAA Paper 91-1826, June 1991.

11. Chu, J. and Lawing, P. L., *"High-Reynolds-Number Test of a 5-Percent-Thick Low-Aspect-Ratio Semispan Wing in the Langley 0.3-Meter Transonic Cryogenic Tunnel - Wing Pressure Distributions,"* NASA TM-4227, December 1990.

12. Vatsa, V.N., "*Accurate Numerical Solutions for Transonic Viscous Flow over Finite Wings,*" Journal of Aricraft, Vol. 24, June 1987, pp. 377-385.

13. Vatsa, V.N. and Wedan, B.W., "*Development of an Efficient Multigrid Code for 3-D Navier-Stokes Equations,*" AIAA Paper 89-1791, June 1989.

14. Murthy, A.V., Johnson, C.B., Ray,E.J., Lawing, P.L., and Thibodeaux, J.J., "*Studies of Sidewall Boundary Layer in the Langley 0.3-Meter Transonic Cryogenic Tunnel With and Without Suction,*" NASA TM-2096, March 1983.

15. Schlichting, H., "*Boundary-Layer Theory,*" 7th ed., McGraw-Hill, New York, 1987.

16. White, F.M., "*Viscous Fluid Flow,*" 1st ed., McGraw-Hill, New York, 1974.

17. Baldwin, B.S. and Lomax, H., "*Thin Layer Approximation and Algebraic Model for Separated Turbulent Flows,*" AIAA Paper 78-257, January 1978.

18. Murthy, A.V., "*An Experimental Study of Wall Adaptation and Interference Assessment Using Cauchy Integral Formula,*" AIAA Paper 91-0399, January 1991.

19. Rebstock, R. and Lee, E. E., "*Capabilities of Wind Tunnels with Two Adaptive Walls to Minimize Boundary Interference in 3-D Model Testing,*" NASA CP-3020, Vol. I, Part 2, 1988, pp. 891-910.

20. Eriksson, L.E., "*Generation of Boundary-Conforming Grids Around Wing-Body Configurations Using Transfinite Interpolation,*" AIAA Journal, Vol. 20, October 1982, pp. 1313-1320.

21. Swanson, R. C. and Turkel, E., "*Artificial Dissipation and Central Difference Schemes for the Euler and Navier-Stokes Equations,*" AIAA Paper 87-1107CP, June 1987.

22. Degani, D. and Schiff, L.B., "*Computation of Supersonic Viscous Flows Around Pointed Bodies at Large Incidence,*" AIAA Paper 83-0034, January 1983.

23. Driver, D.M., "*Reynolds Shear Stress Measurements in a Separated Boundary Layer Flow,*" AIAA Paper 91-1787, June 1991.

24. Liu, X. and Squire, L.C., "*An Investigation of Shock/Boundary-Layer Interactions on Curved Surfaces at Transonic Speeds,*" Journal of Fluid Mechanics, Vol. 187, 1988, pp. 467-486.

25. Anderson, E.C. and Lewis, C.H., "*Laminar or Turbulent Boundary-Layer Flows of Perfect Gases or Reacting Gas Mixtures in Chemical Equilibrium.*" NASA CR-1893, 1971.

9 Figures

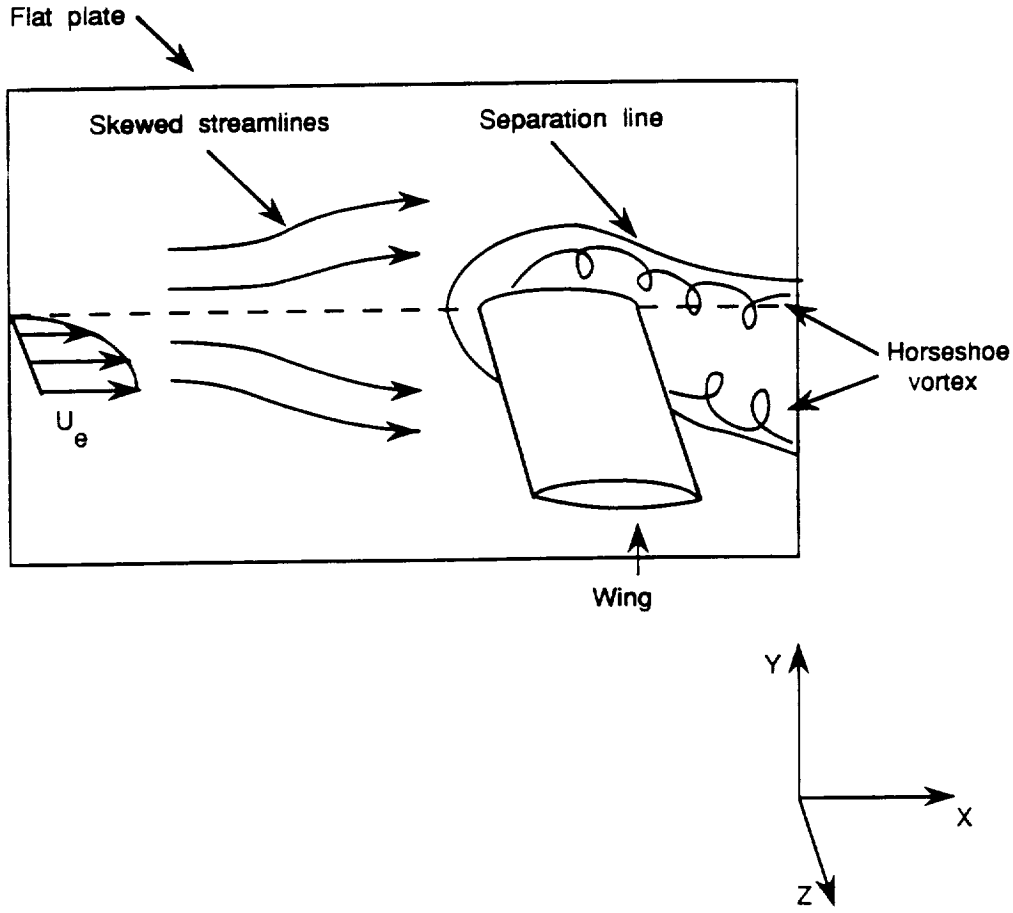

Fig. 1: Juncture flow physics.

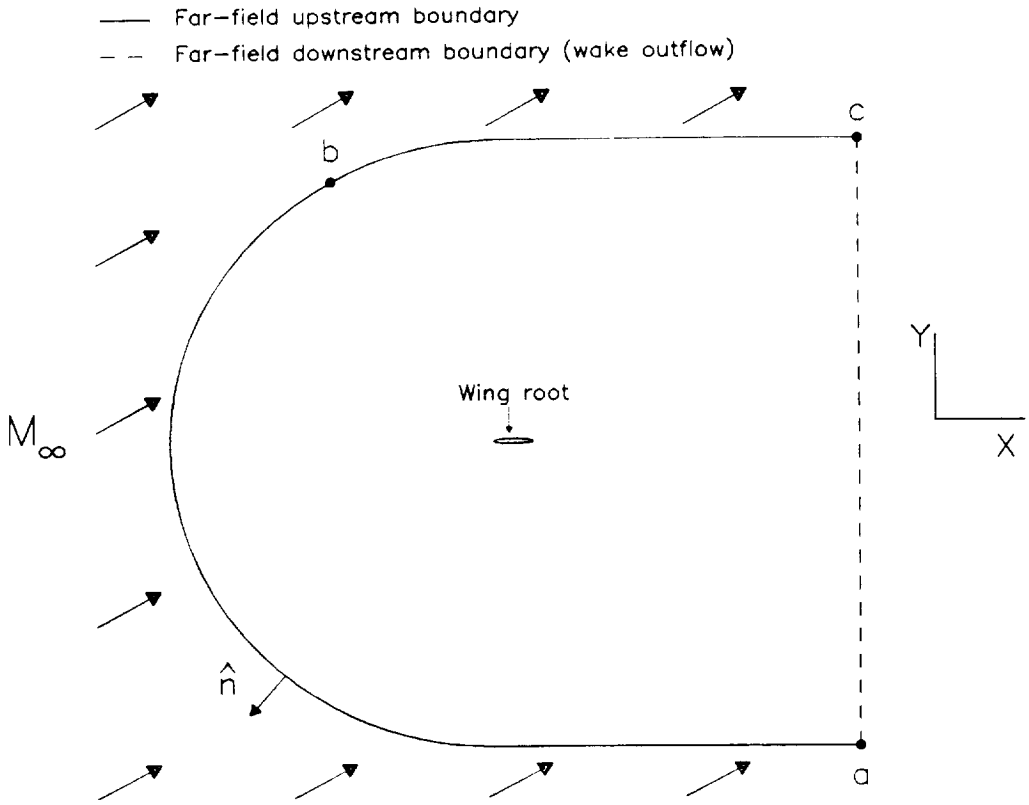

Fig. 2: Schematic of far-field boundary conditions.

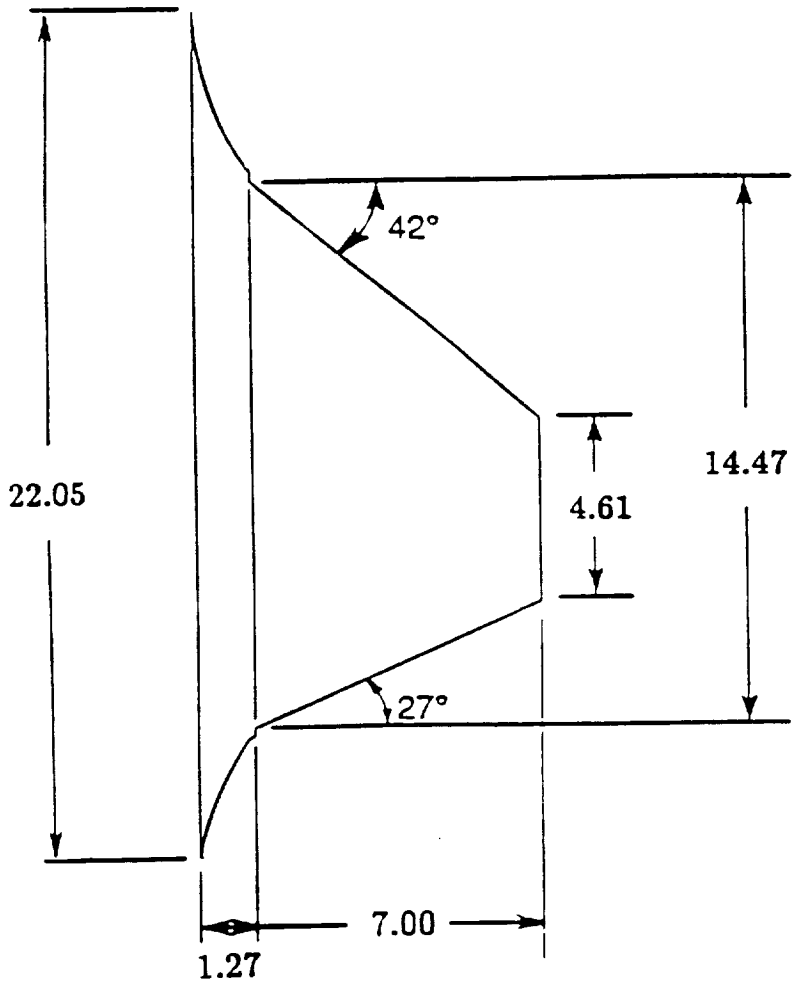

Fig. 3: Planform view of wing geometry (dimensions in centimeters).

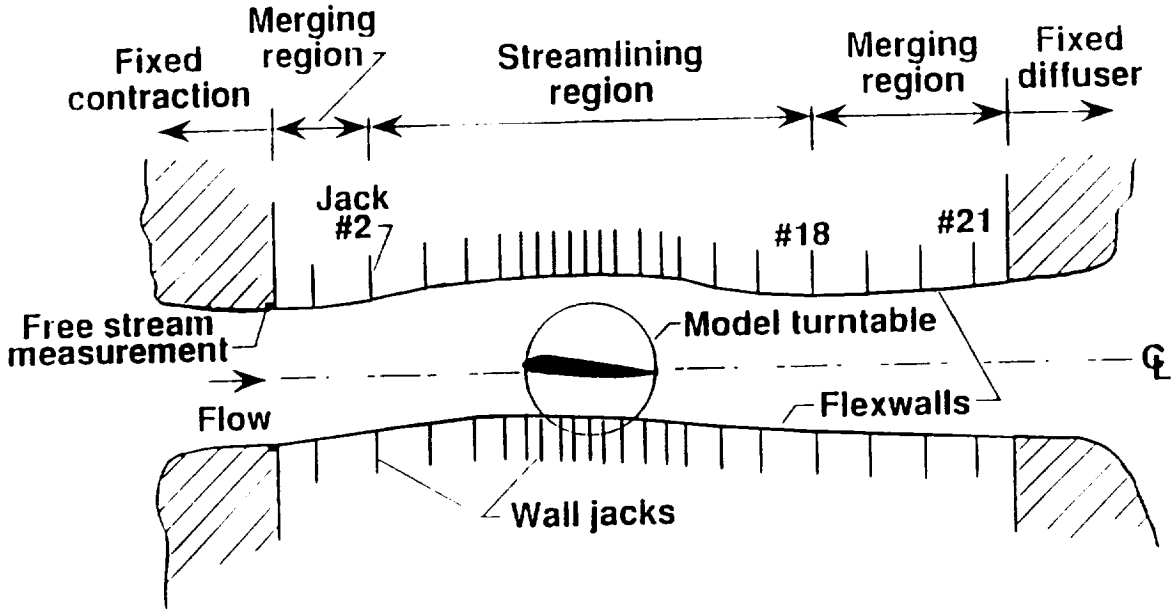

Fig. 4: Schematic of adaptive wall test section.

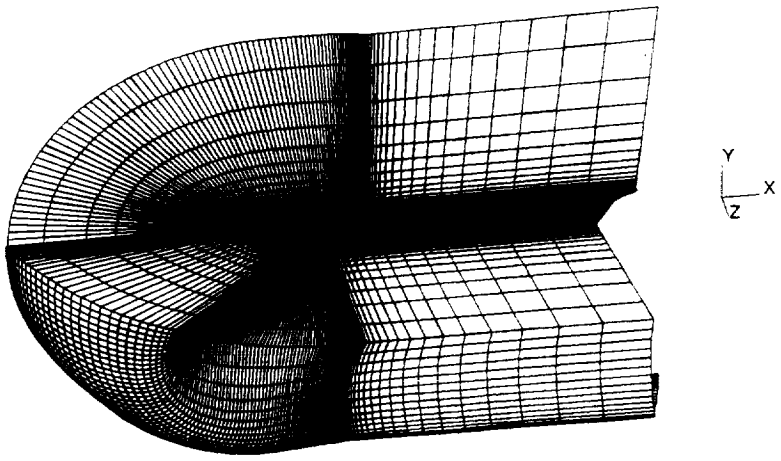

a) viscous sidewall grid

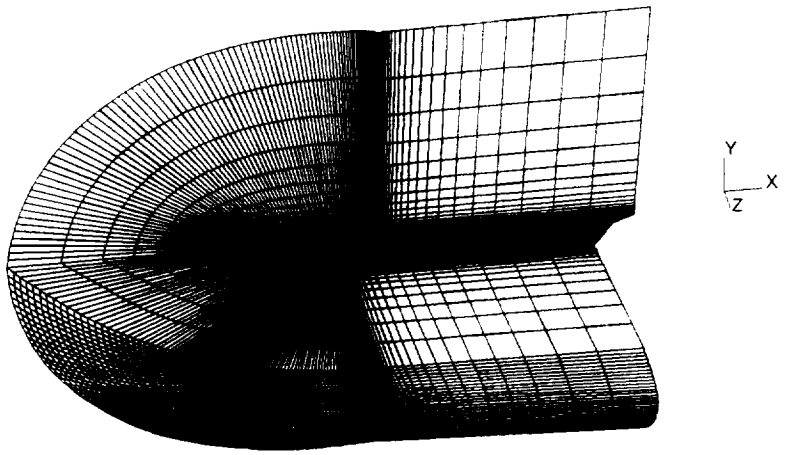

b) free-air grid

Fig. 5: Partial view of C-O mesh topologies.

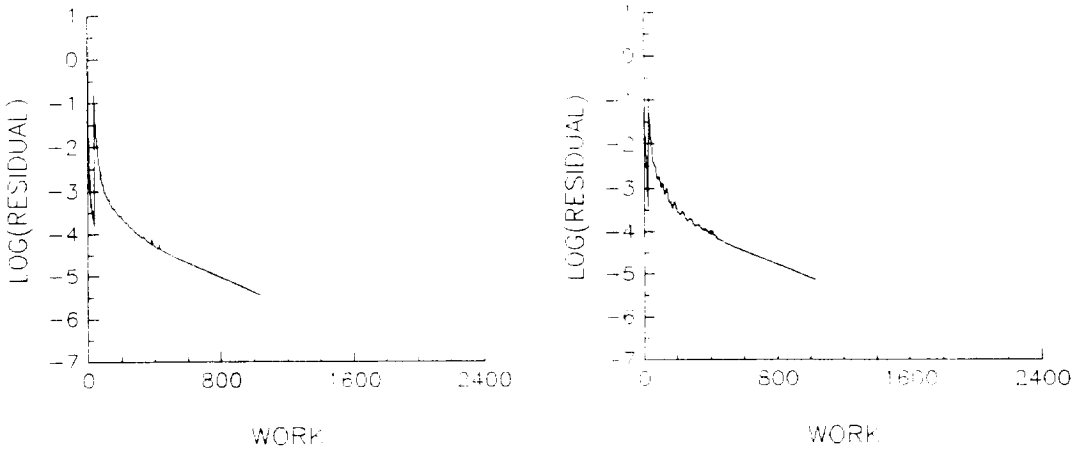

a) 97×33×25

b) 193×33×25

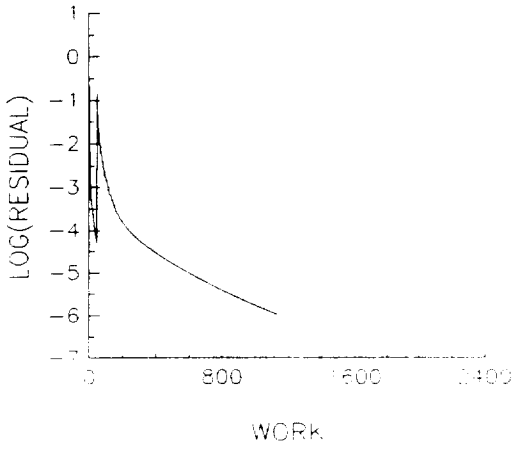

c) 241×49×25

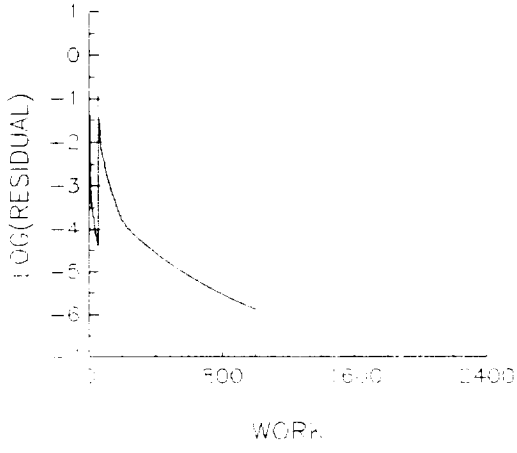

d) 241×49×49

Fig. 6: Effects of grid refinement on convergence histories ($M_\infty = .70$, $\alpha = 8.24°$, Re = high).

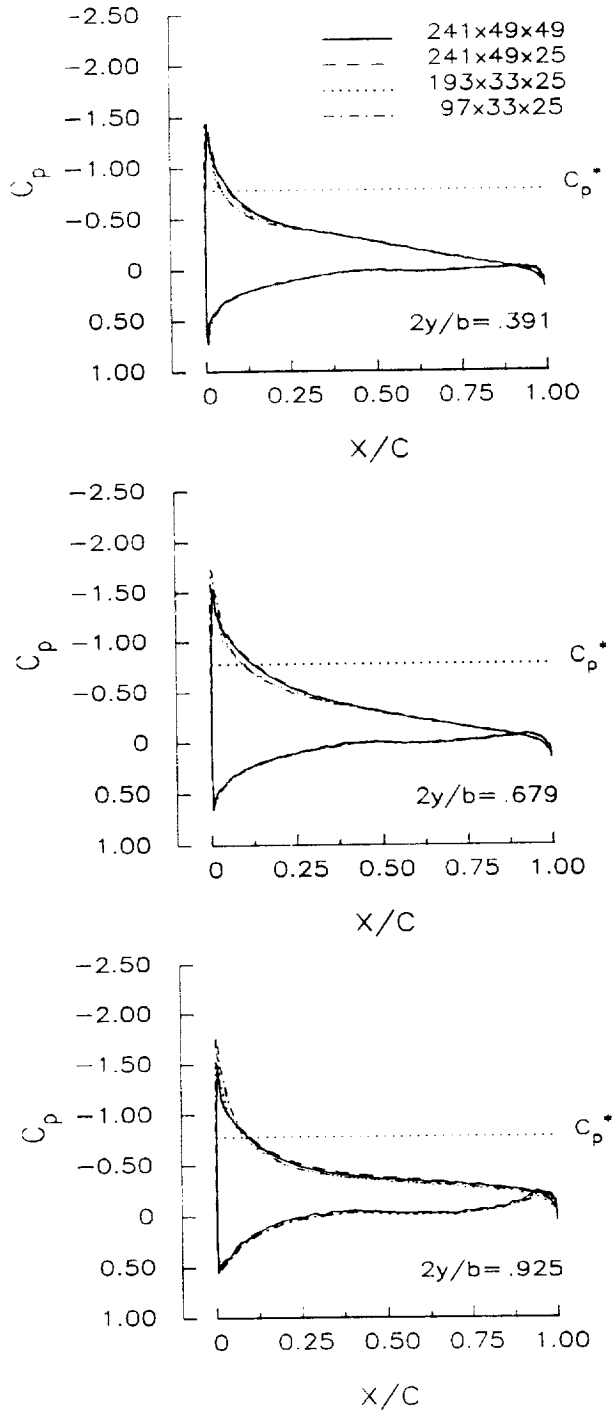

Fig. 7: Effects of grid refinement on pressure distribution ($M_\infty = .70$, $\alpha = 8.24°$, Re = high).

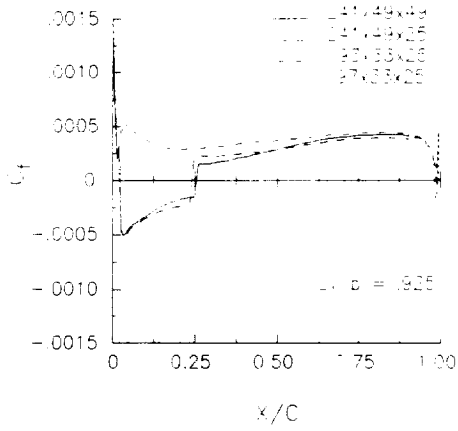

a) skin-friction distribution

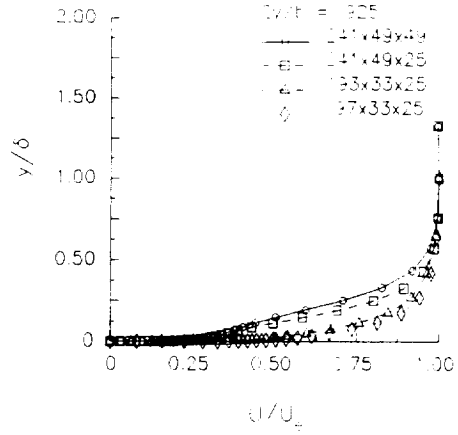

b) chordwise velocity profiles

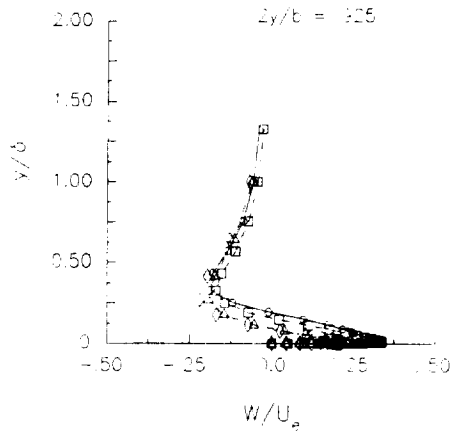

c) spanwise velocity profiles

Fig. 8: Effects of grid refinement on outboard section flow field ($M_\infty = .70$, $\alpha = 8.24°$, Re = high).

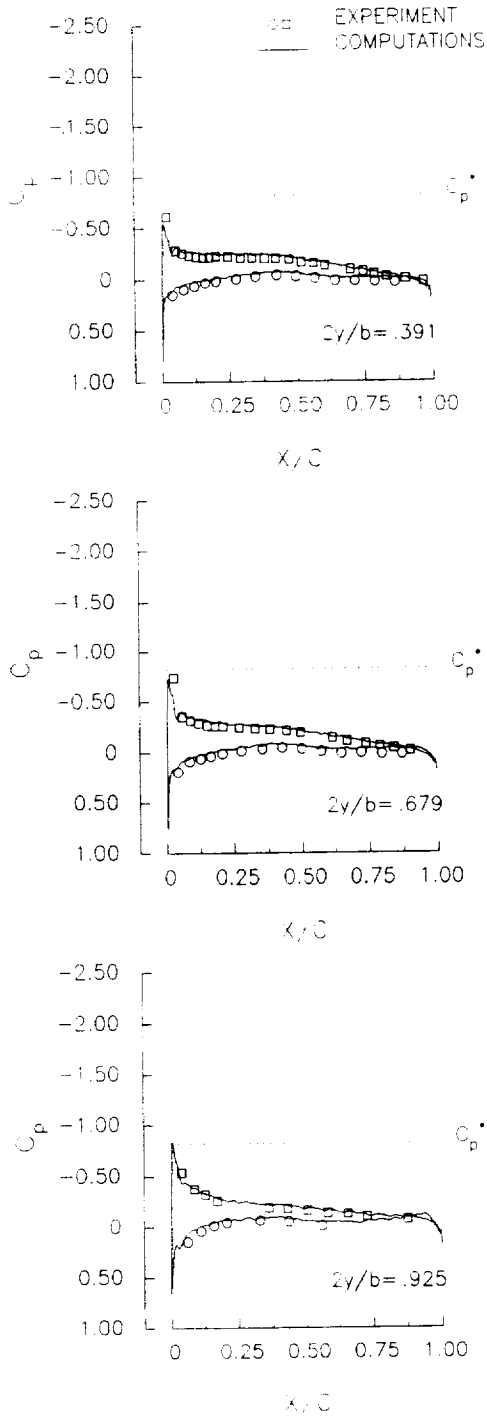

Fig. 9: Comparison of computational results to experimental data ($M_\infty = .70$, $\alpha = 3.17°$, Re = medium).

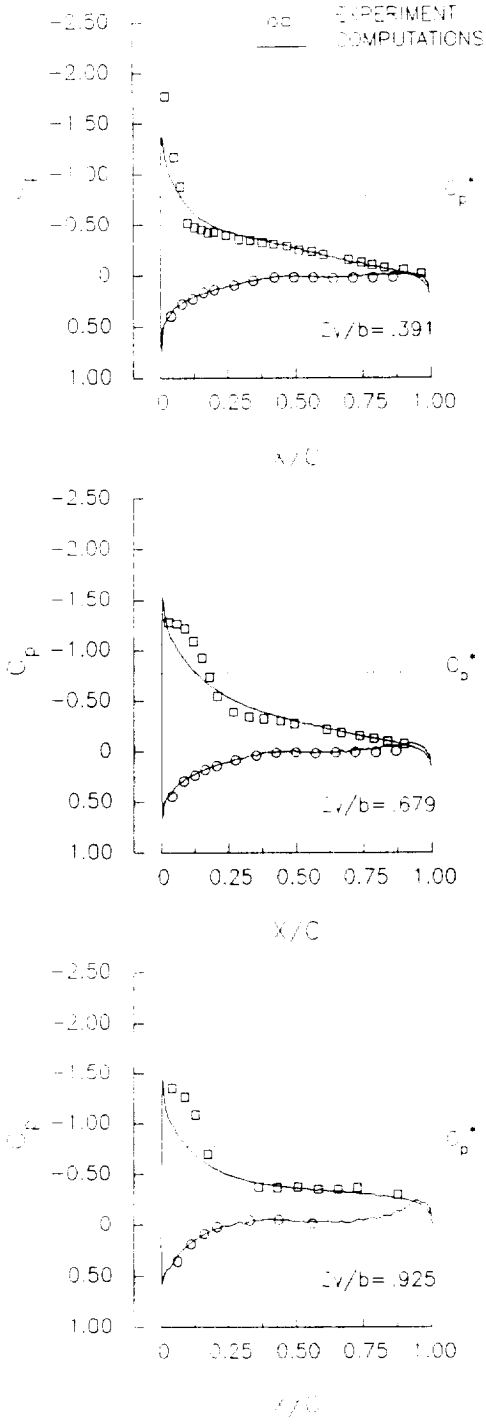

Fig. 10: Comparison of computational results to experimental data ($M_\infty = .70$, $\alpha = 8.24°$, Re = medium).

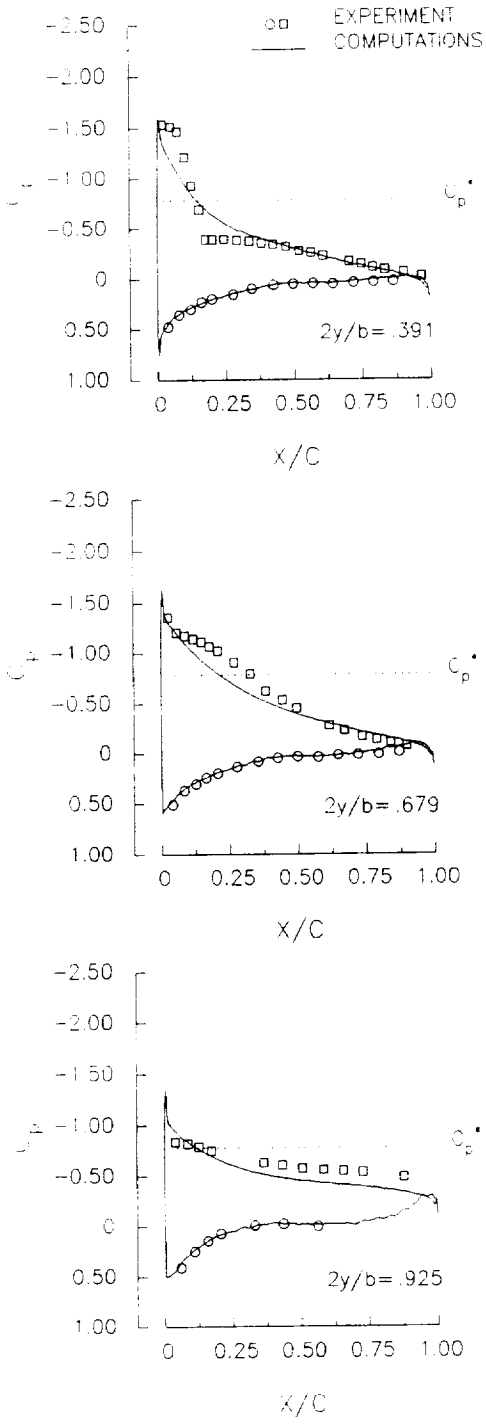

Fig. 11: Comparison of computational results to experimental data ($M_\infty = .70$, $\alpha = 10.25°$, Re = medium).

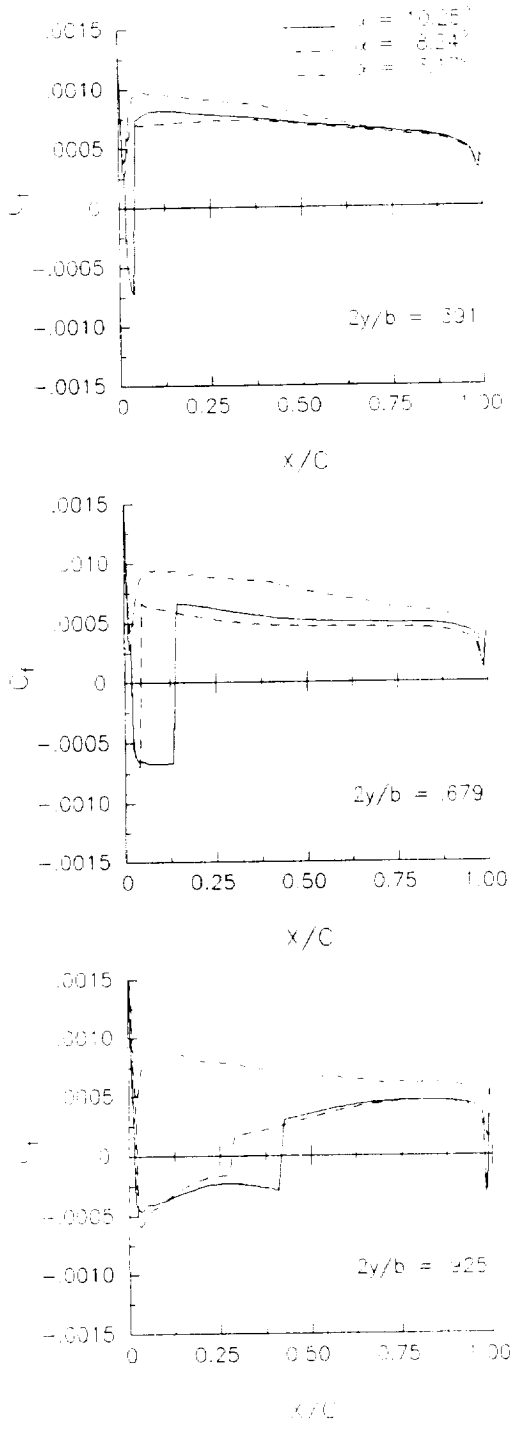

Fig. 12: Effect of angle of attack on computed skin-friction distributions on upper wing surface ($M_\infty = .70$, Re = medium).

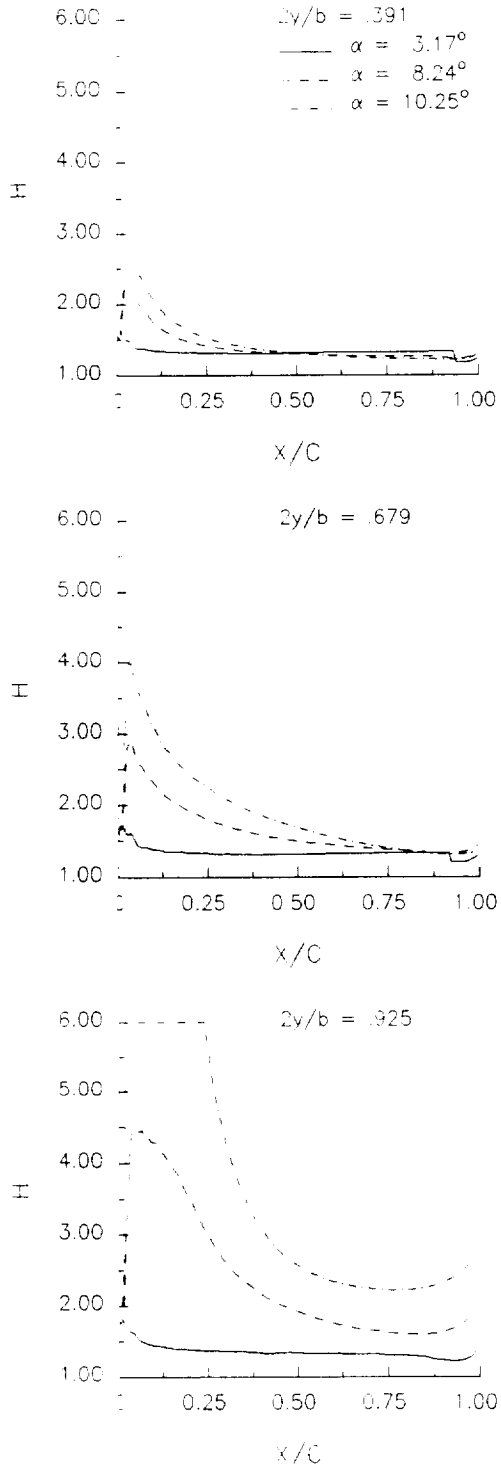

Fig. 13: Effect of angle of attack on computed shape factor distributions on upper wing surface ($M_\infty = .70$, Re = medium).

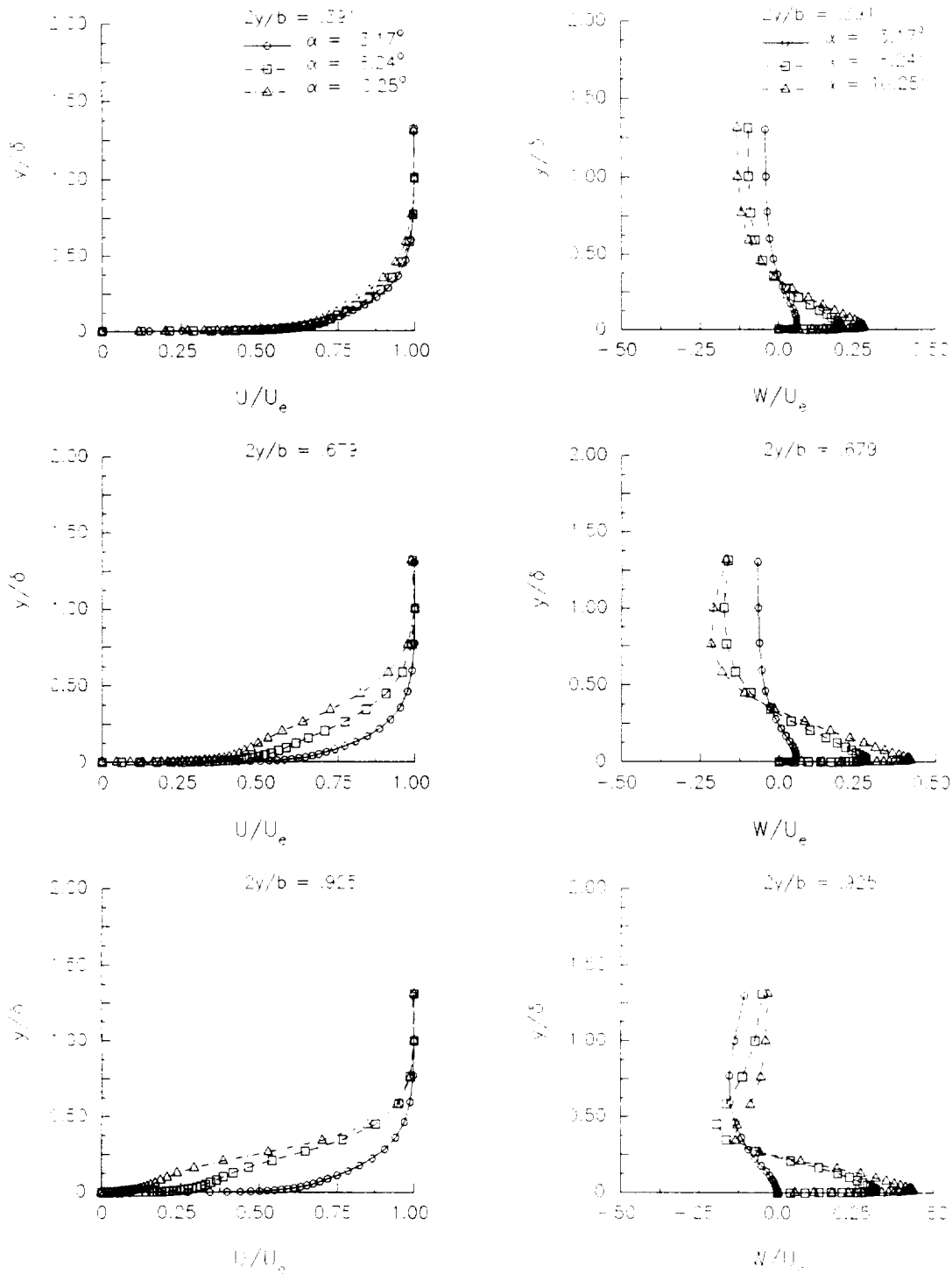

a) chordwise profiles

b) spanwise profiles

Fig. 14: Effect of angle of attack on velocity profiles for upper surface, 50%chord (M_∞ = .70, Re = medium).

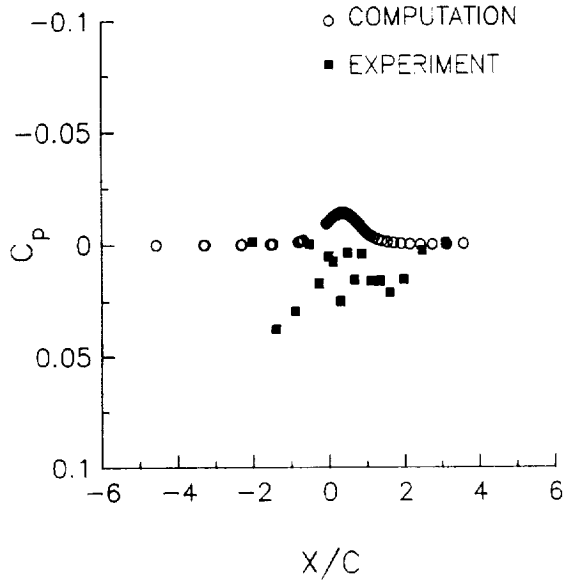

a) upper wall

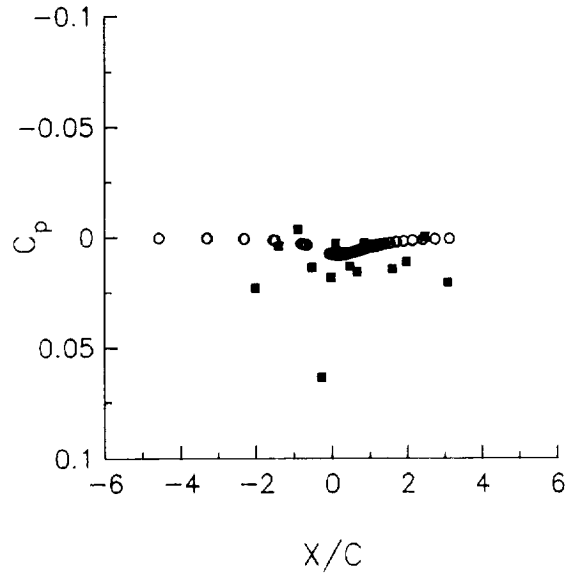

b) lower wall

Fig. 15: Comparison between experimental and computed pressure distributions along centerline of flexible walls ($M_\infty = .70$, $\alpha = 8.24°$, Re = high).

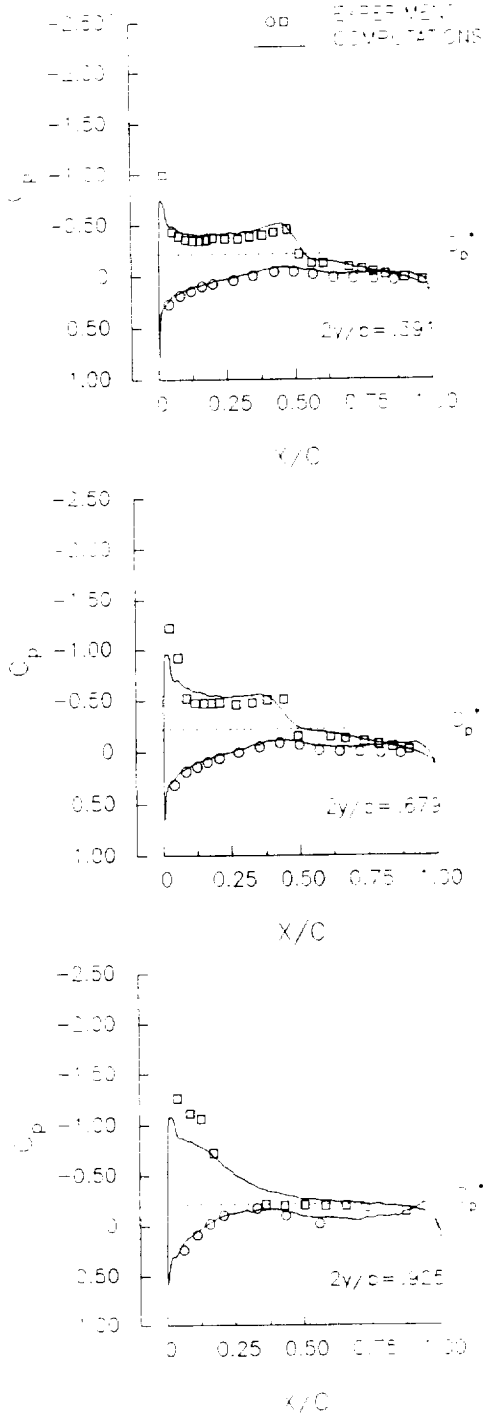

Fig. 16: Comparison of computational results to experimental data (M_∞ = .8860, α = 5.46°, Re = medium).

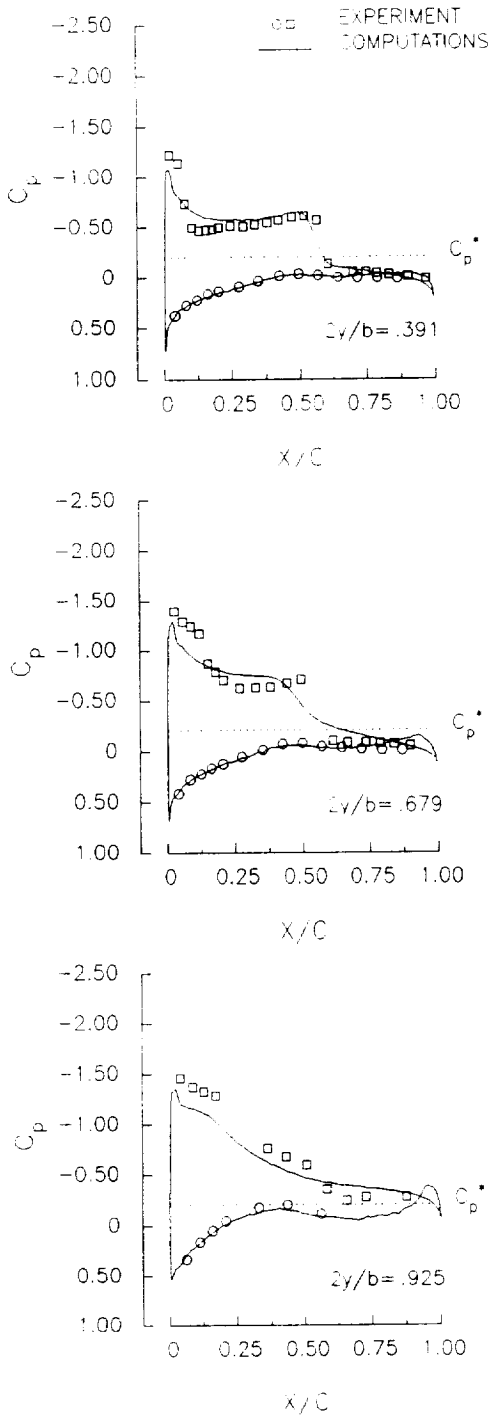

Fig. 17: Comparison of computational results to experimental data (M_∞ = .8920, α = 8.55°, Re = medium).

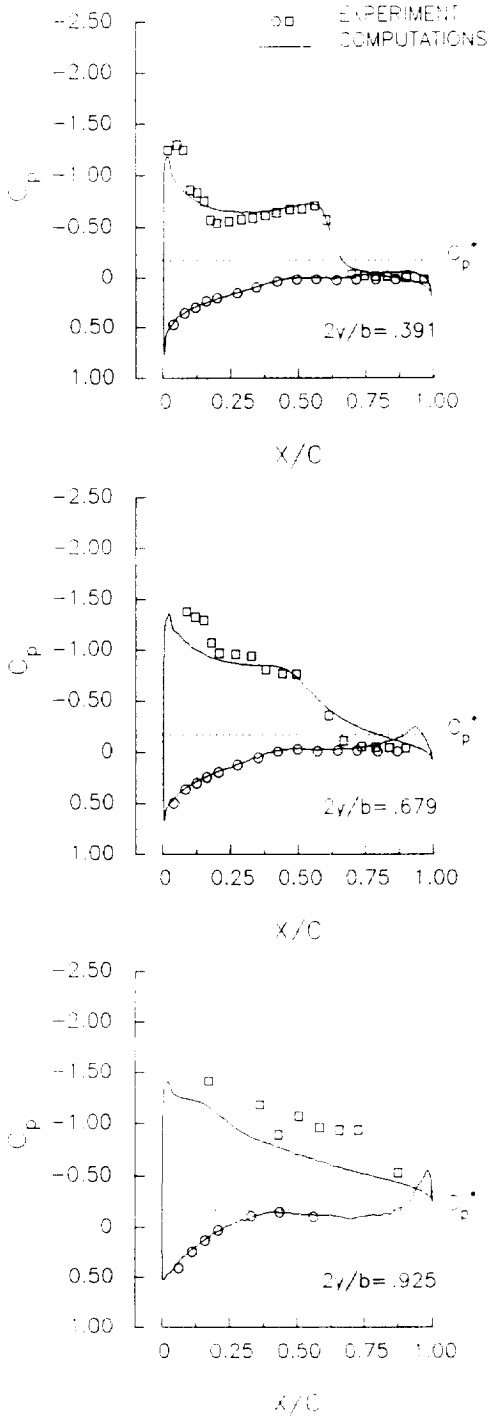

Fig. 18: Comparison of computational results to experimental data (M_∞ = .9073, α = 10.31°, Re = medium).

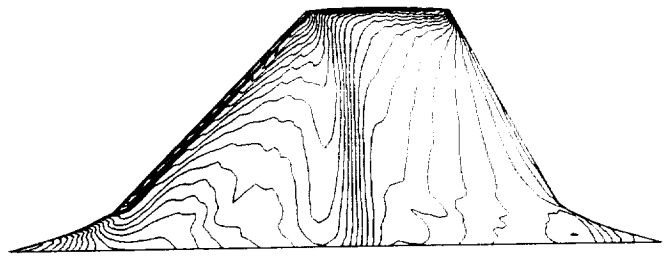

a) $\alpha = 5.46°$

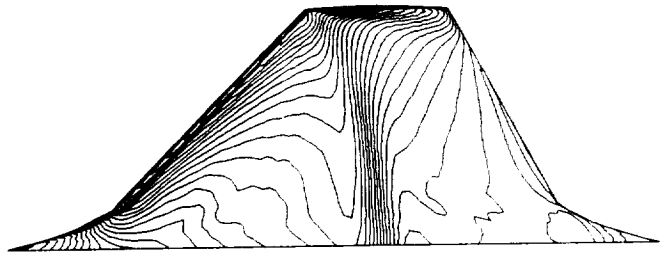

b) $\alpha = 8.55°$

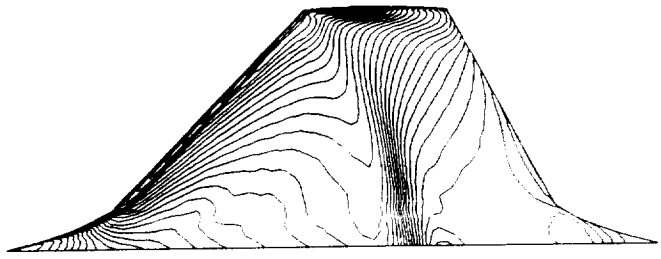

c) $\alpha = 10.31°$

Fig. 19: Effect of angle of attack on computed upper surface pressure contours ($M_\infty \approx .90$,Re = medium).

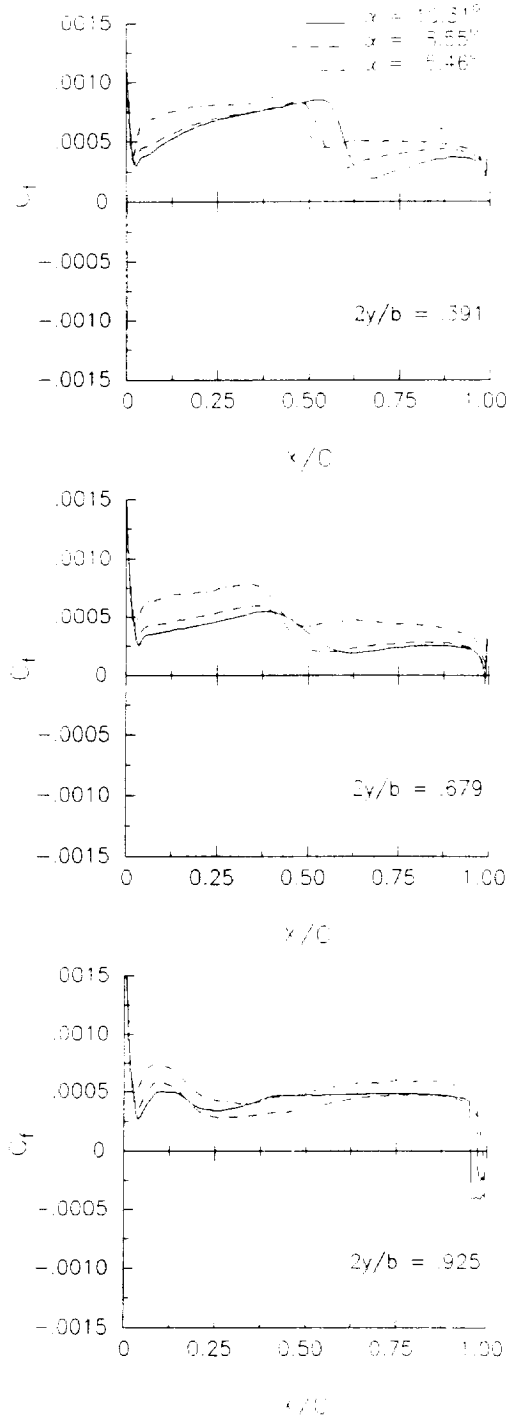

Fig. 20: Effect of angle of attack on computed skin-friction distributions on upper wing surface ($M_\infty \approx .90$, Re = medium).

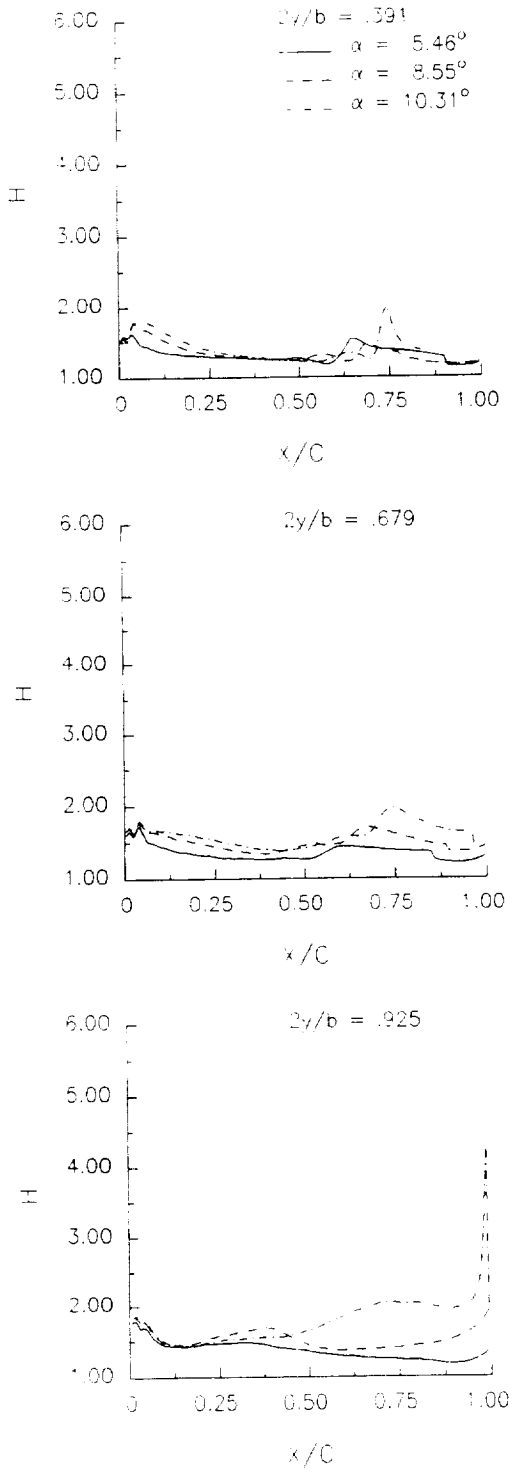

Fig. 21: Effect of angle of attack on computed shape factor distributions on upper wing surface ($M_\infty \approx .90$, Re = medium).

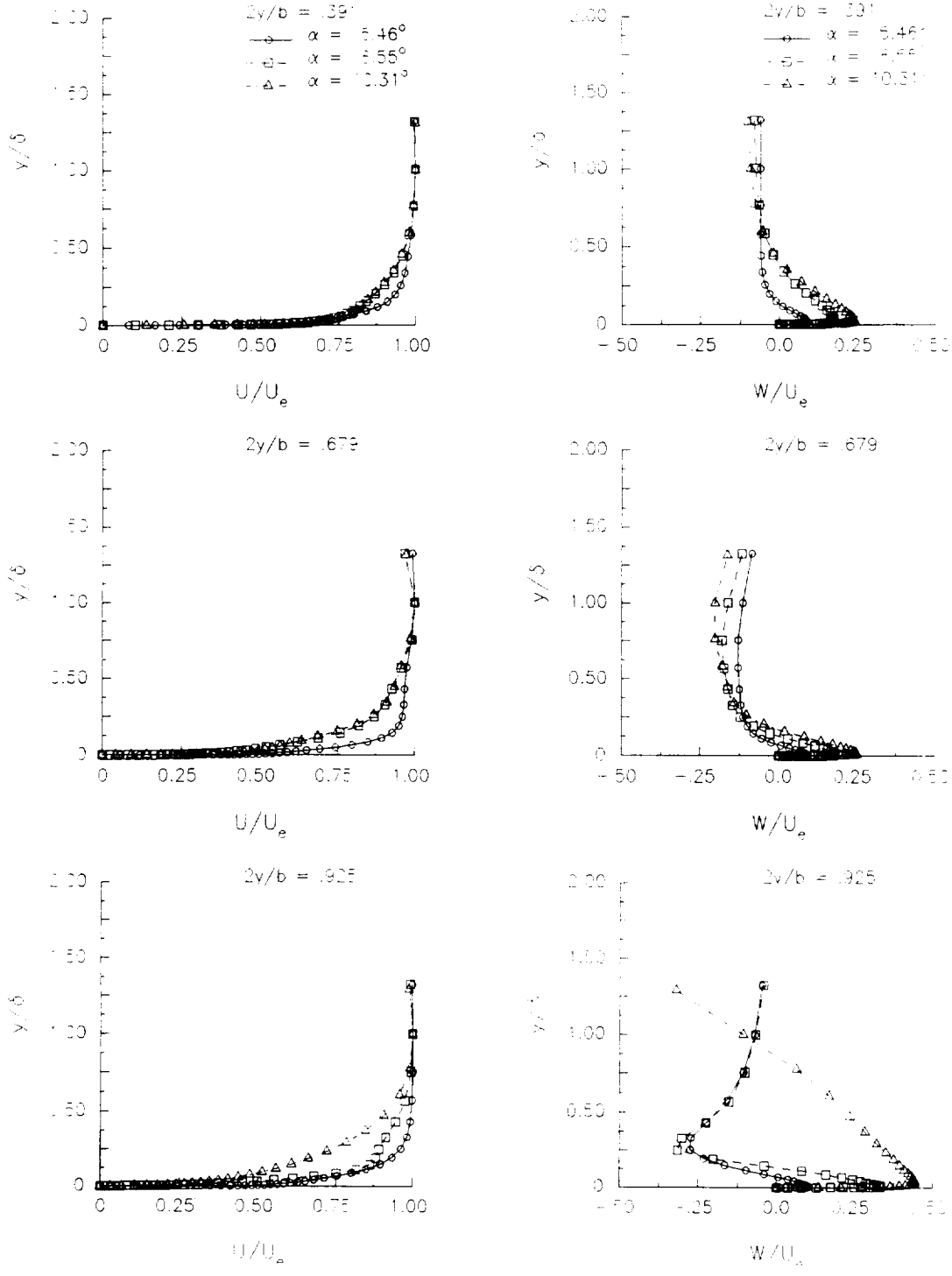

a) chordwise profiles

b) spanwise profiles

Fig. 22: Effect of angle of attack on velocity profiles for upper surface, 50% chord ($M_\infty \approx .90$, Re = medium).

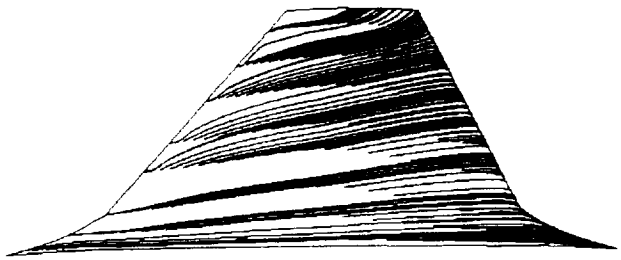

a) $\alpha = 5.46°$

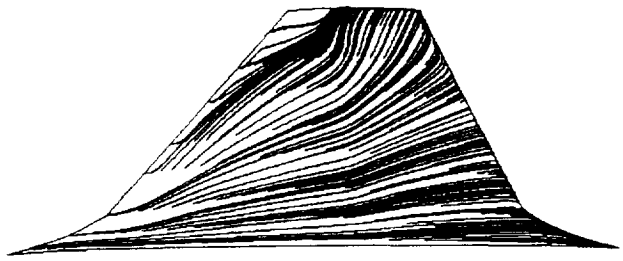

b) $\alpha = 8.55°$

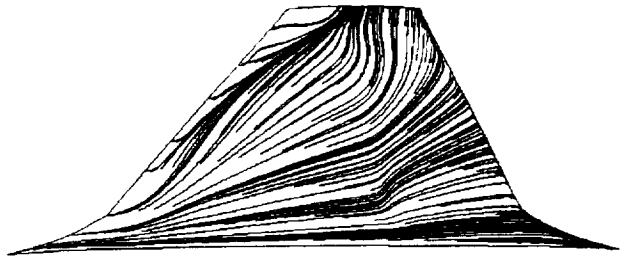

c) $\alpha = 10.31°$

Fig. 23: Effect of angle of attack on computed upper surface streamline patterns ($M_\infty \approx .90$, Re = medium).

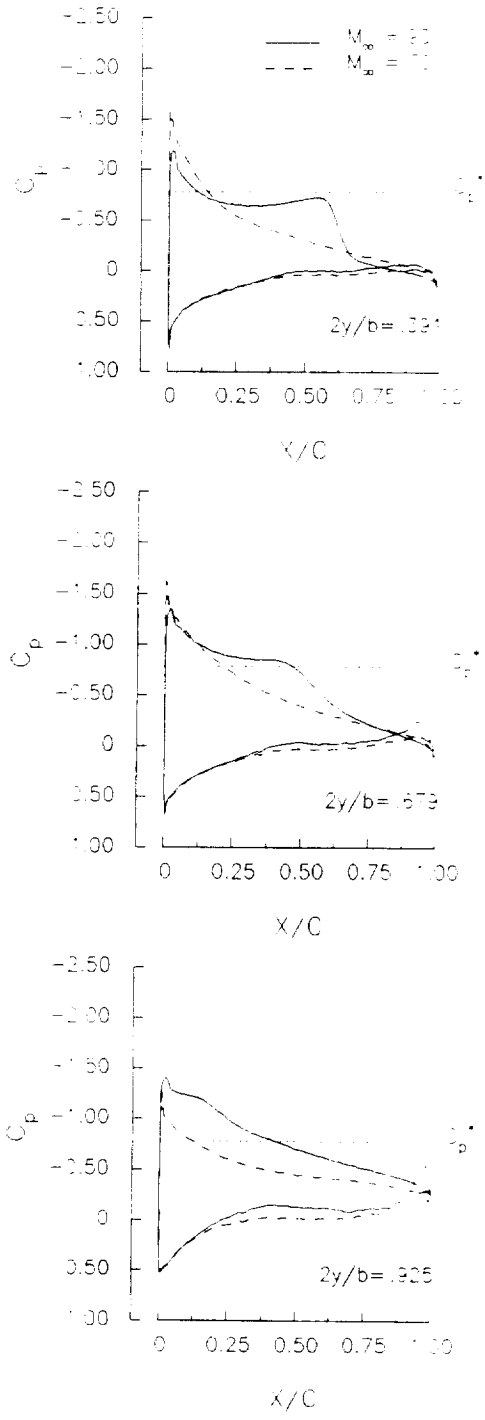

Fig. 24: Effect of freestream Mach number on computed pressure distribution ($\alpha \approx$ 10.0°, Re= medium).

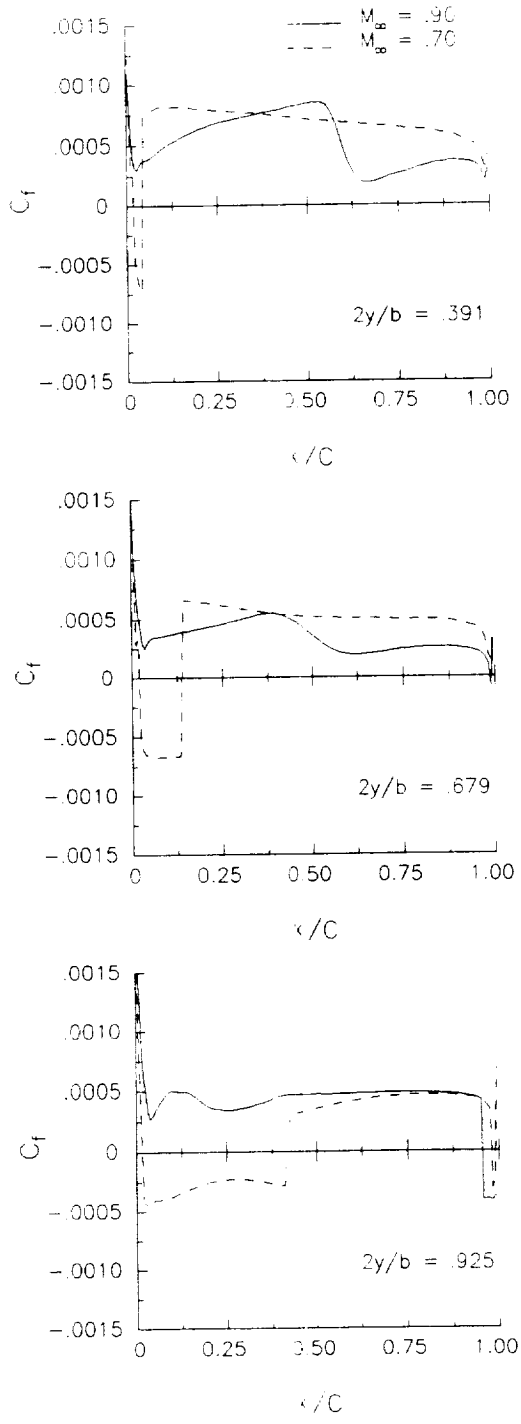

Fig. 25: Effect of freestream Mach number on computed skin-friction distribution ($\alpha \approx 10.0°$, Re = medium).

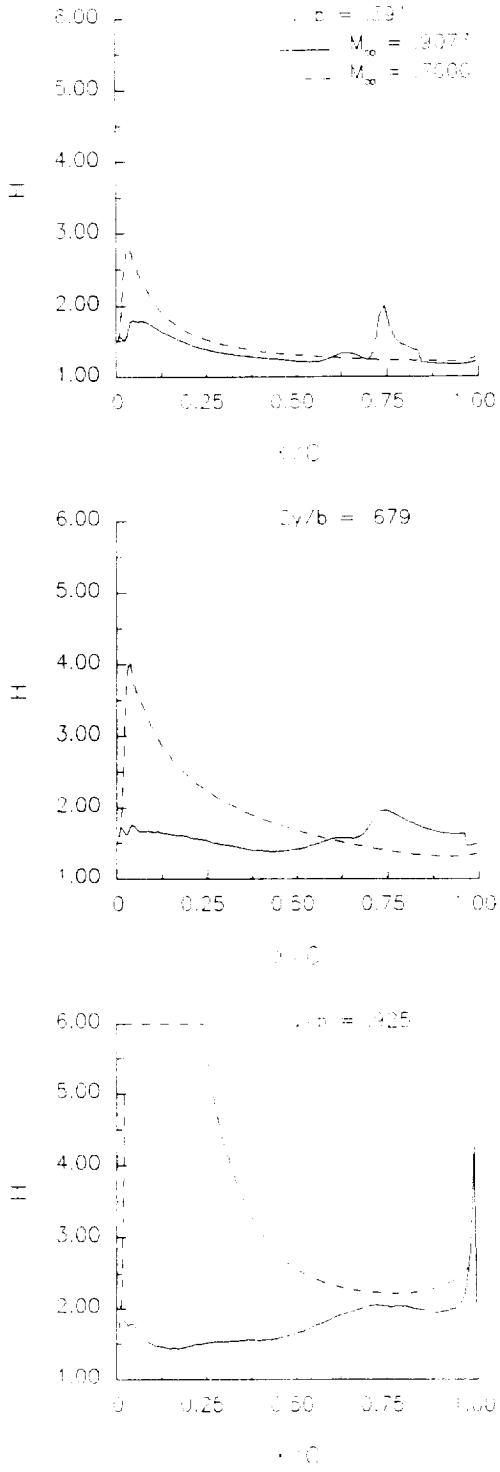

Fig. 26: Effect of freestream Mach number on computed shape factor distribution ($\alpha \approx 10.0°$, Re = medium).

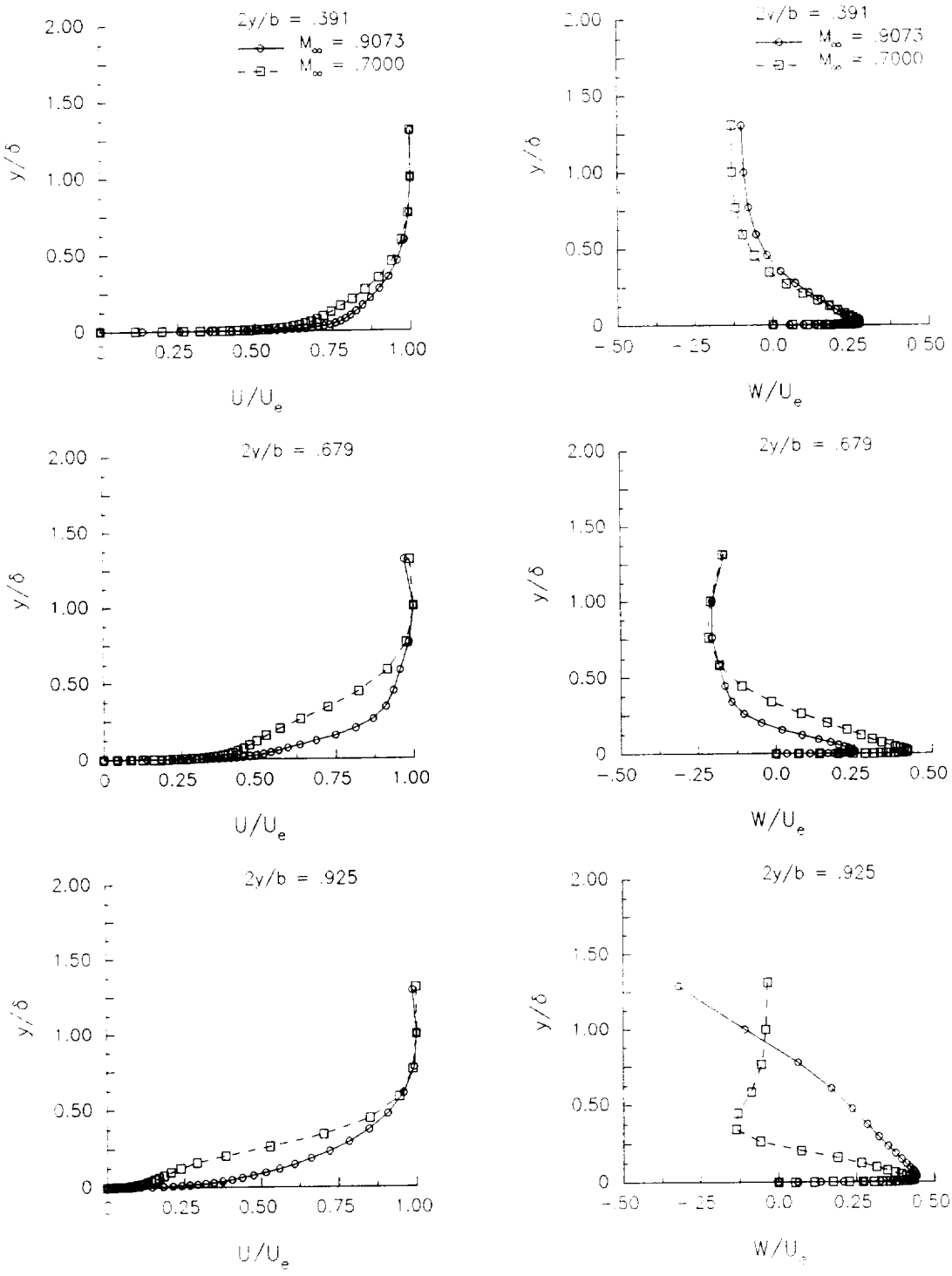

a) chordwise profiles

b) spanwise profiles

Fig. 27: Effect of freestream Mach number on velocity profiles, 50%chord ($\alpha \approx$ 10.0°, Re = medium).

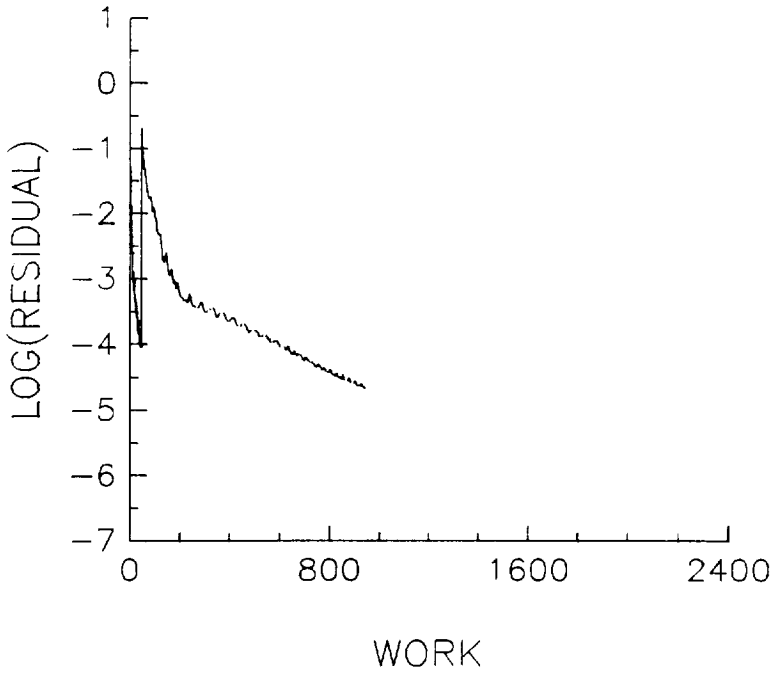

Fig. 28: Convergence history for viscous sidewall computation, $241 \times 65 \times 49$ grid ($M_\infty = .70, \alpha = 8.24°$, Re = medium).

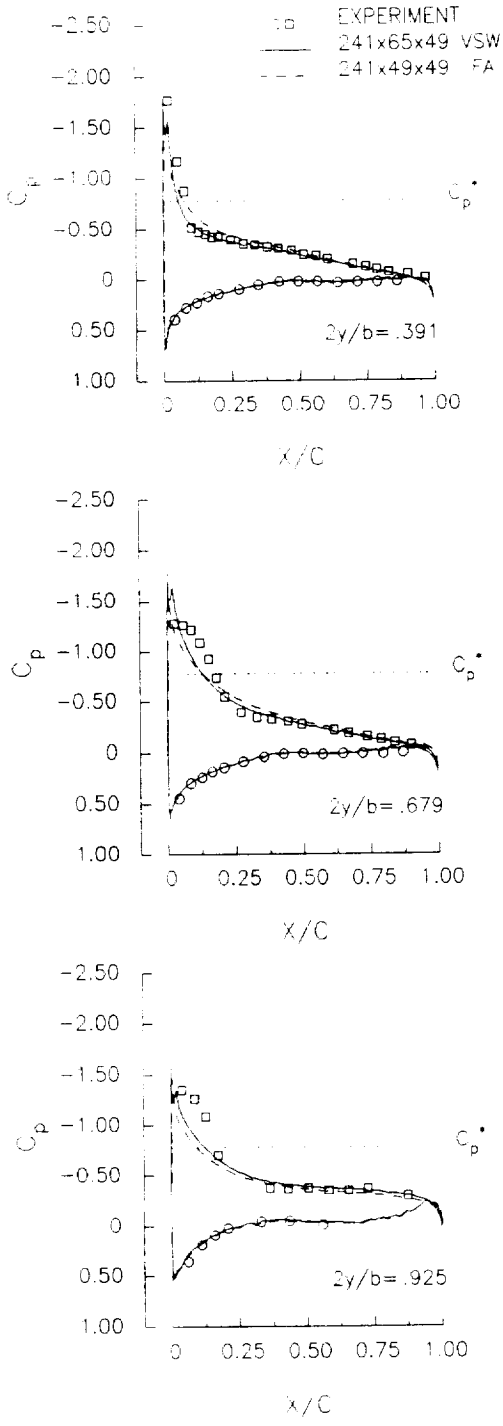

Fig. 29: Influence of sidewall boundary layer on wing surface pressure distribution ($M_\infty = .70$, $\alpha = 8.24°$, Re = medium).

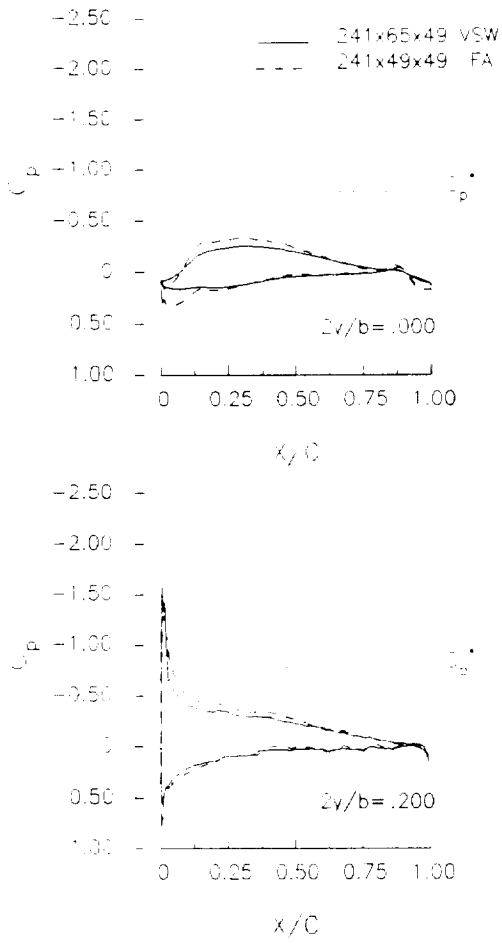

Fig. 30: Influence of sidewall boundary layer on fillet surface pressure distribution ($M_\infty = .70$, $\alpha = 8.24°$, Re = medium).

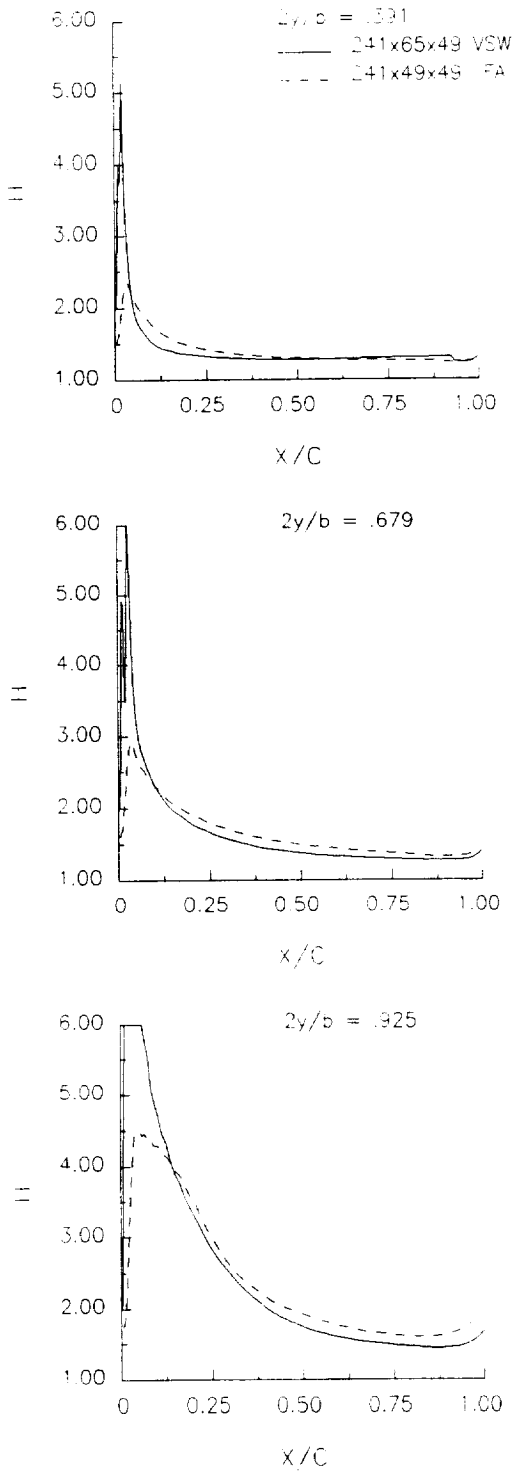

Fig. 31: Influence of sidewall boundary layer on computed shape factor distributions ($M_\infty = .70$, $\alpha = 8.24°$, Re = medium).

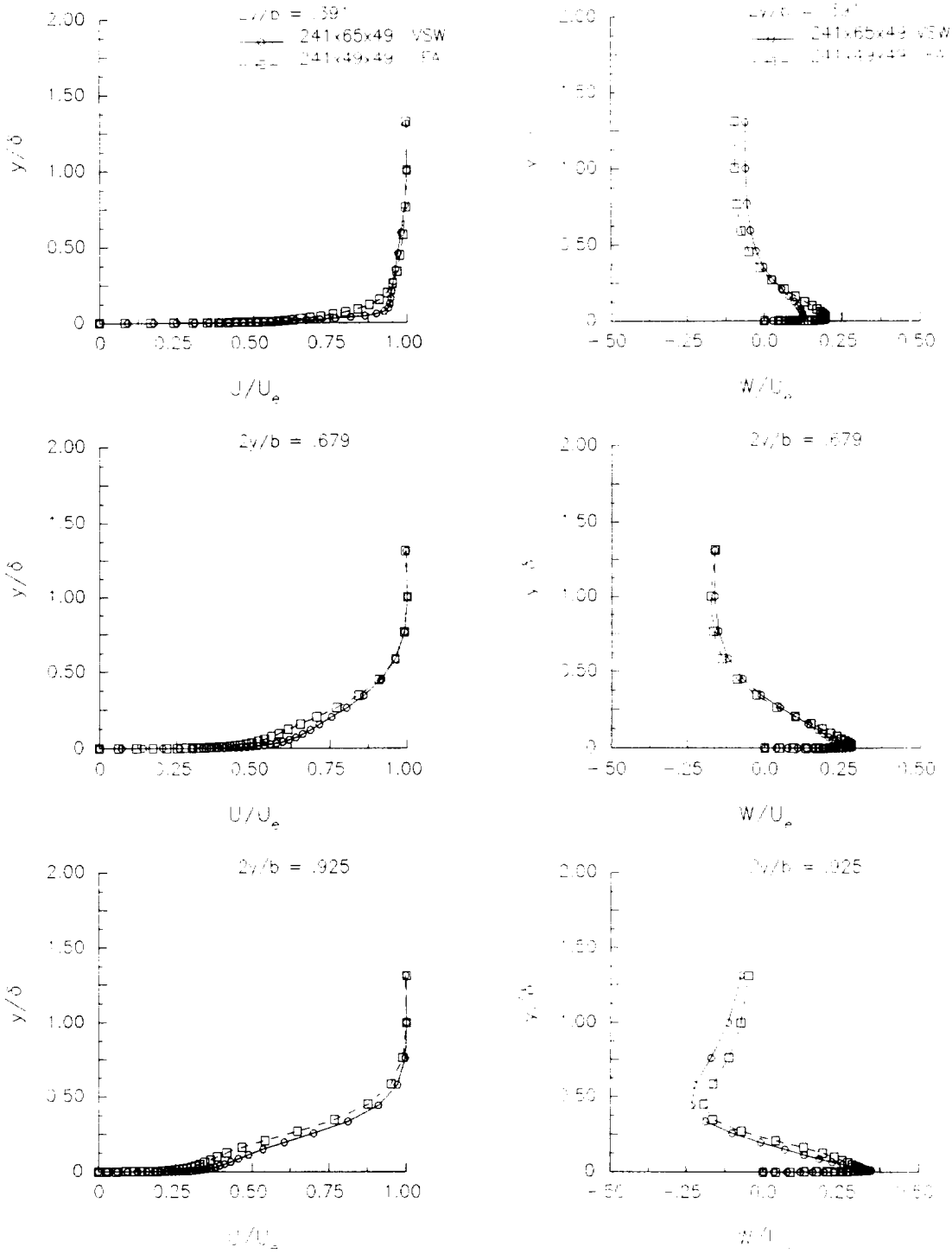

a) chordwise profiles

b) spanwise profiles

Fig. 32: Influence of sidewall boundary layer on velocity profiles for upper surface, 50%chord ($M_\infty = .70$, $\alpha = 8.24°$, Re = medium).

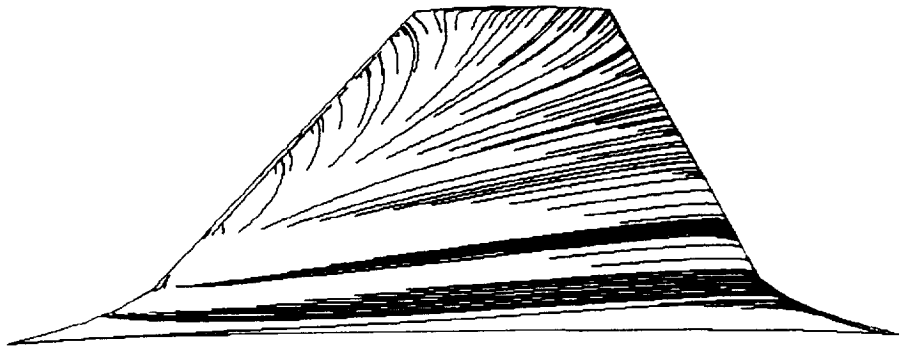

a) viscous sidewall computation

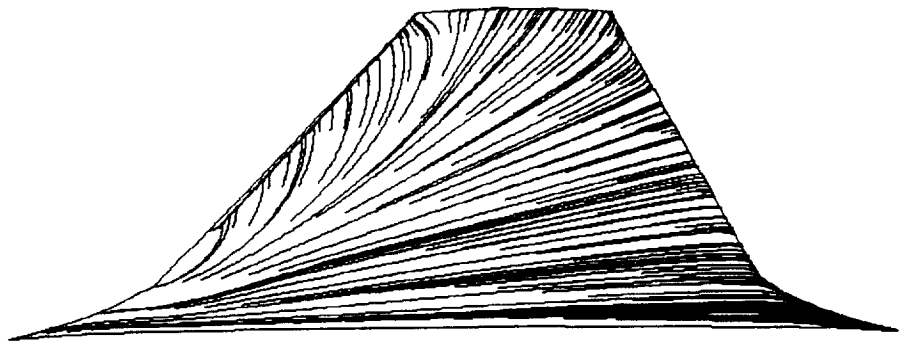

b) free-air computation

Fig. 33: Influence of sidewall boundary layer on wing streamline pattern (M_∞ = .70, α = 8.24°, Re = medium).

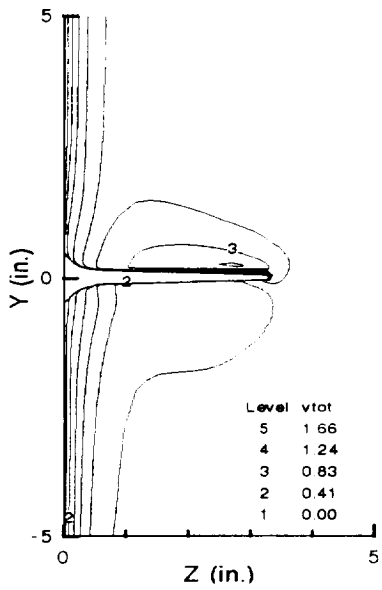

a) 25% chord

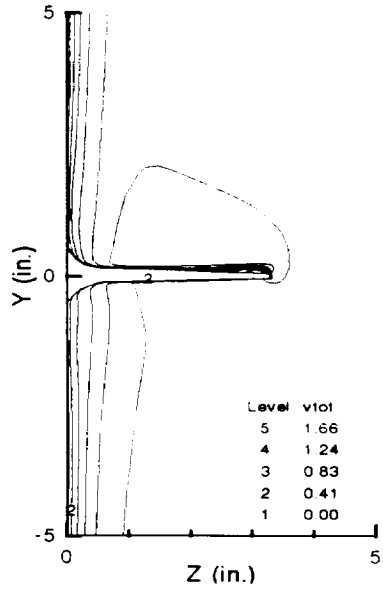

b) 50%chord

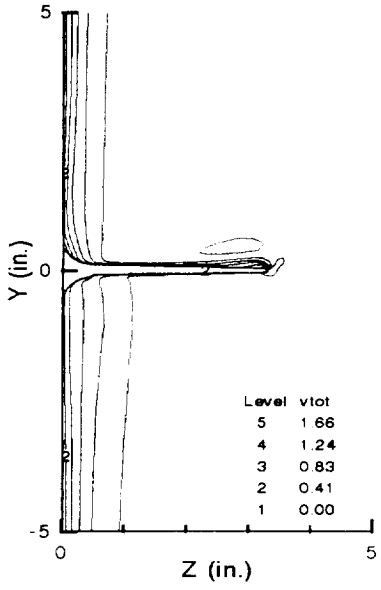

c) 75% chord

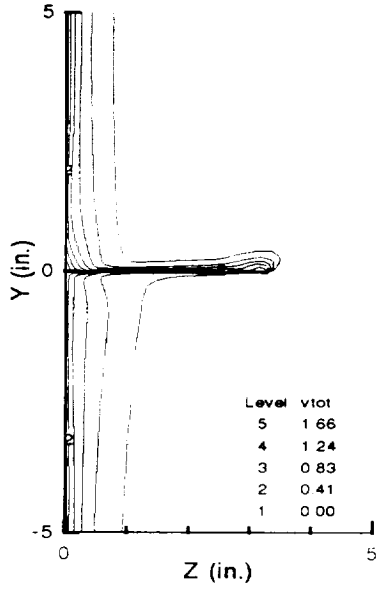

d) trailing edge

Fig. 34: Total velocity contours for viscous sidewall computation ($M_\infty = .70$, $\alpha = 8.24°$, Re = medium).

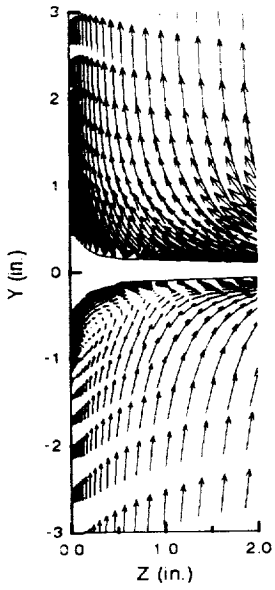

a) 25% chord

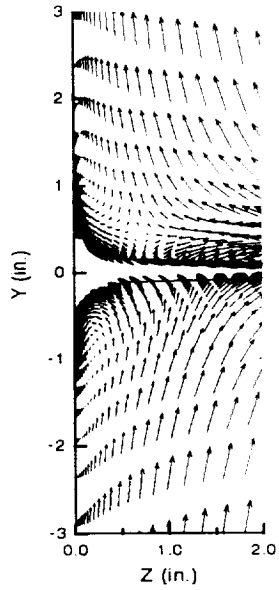

b) 50%chord

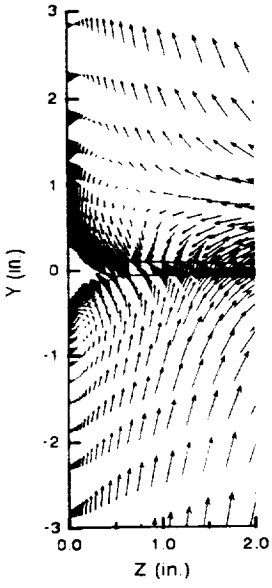

c) 75% chord

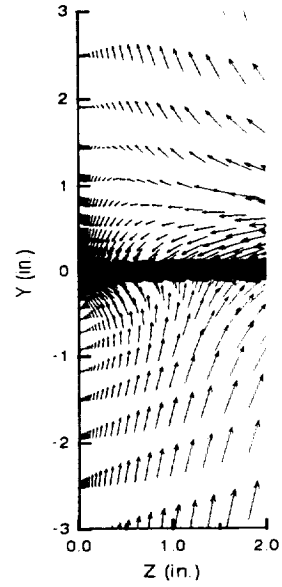

d) trailing edge

Fig. 35: Cross-flow velocity vectors, viscous sidewall computation ($M_\infty = .70$, $\alpha = 8.24°$, Re = medium).

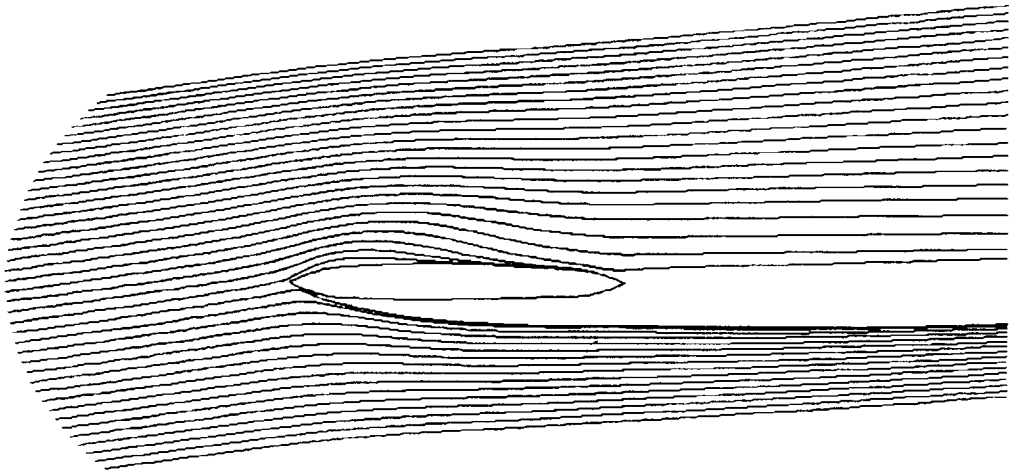

a) viscous sidewall computation

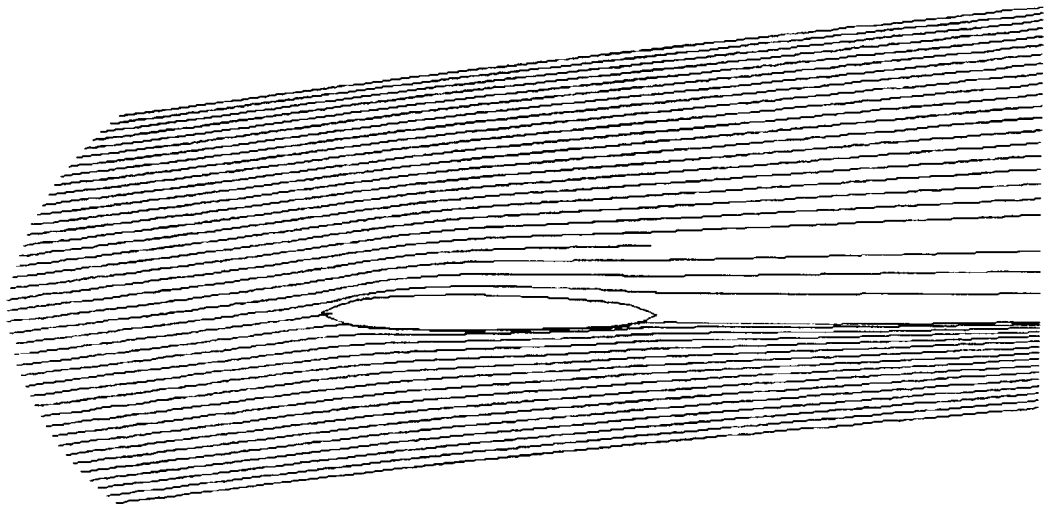

b) free-air computation

Fig. 36: Influence of sidewall boundary layer on root plane streamline pattern (M_∞ = .70, α = 8.24°, Re = medium).

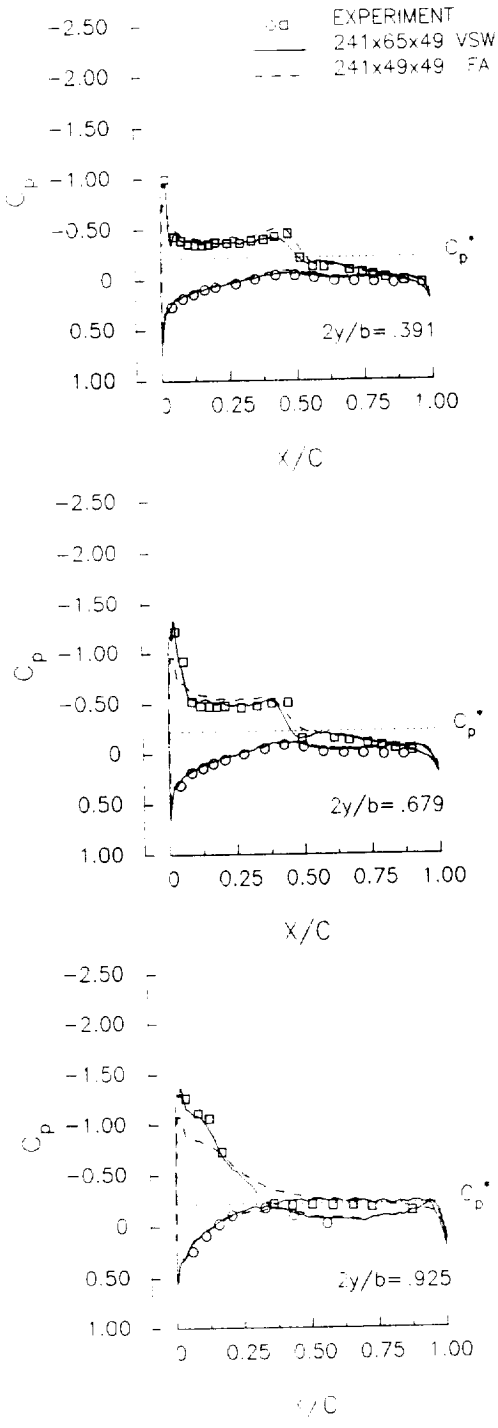

Fig. 37: Influence of sidewall boundary layer on wing surface pressure distribution ($M_\infty = .8860$, $\alpha = 5.46°$, Re= medium).

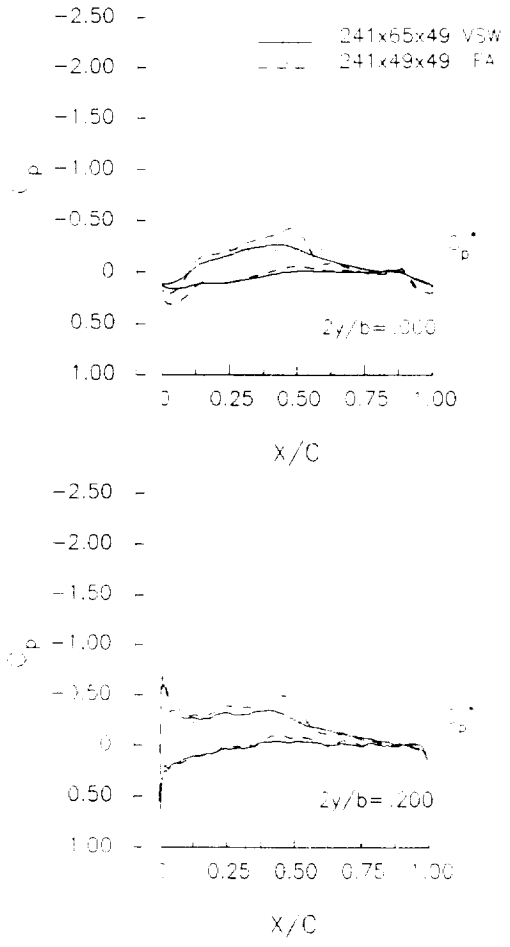

Fig. 38: Influence of sidewall boundary layer on fillet surface pressure distribution ($M_\infty = .8860$, $\alpha = 5.46°$, Re = medium).

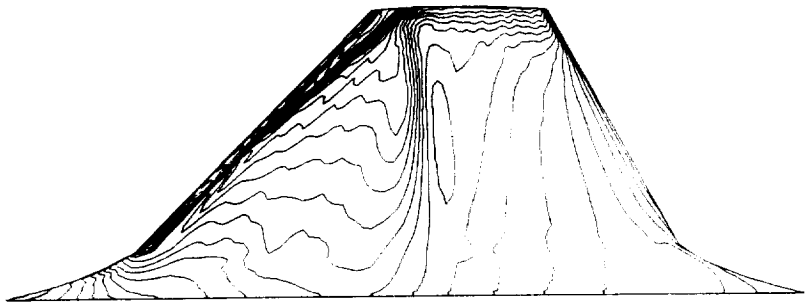

a) viscous sidewall computation

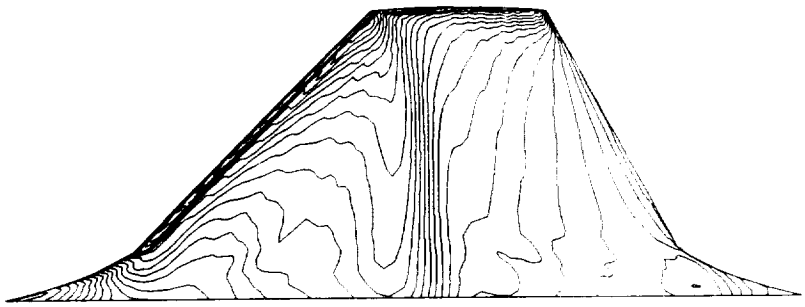

b) free-air computation

Fig. 39: Influence of sidewall boundary layer on computed surface pressure contours ($M_\infty = .8860$, $\alpha = 5.46°$, Re = medium).

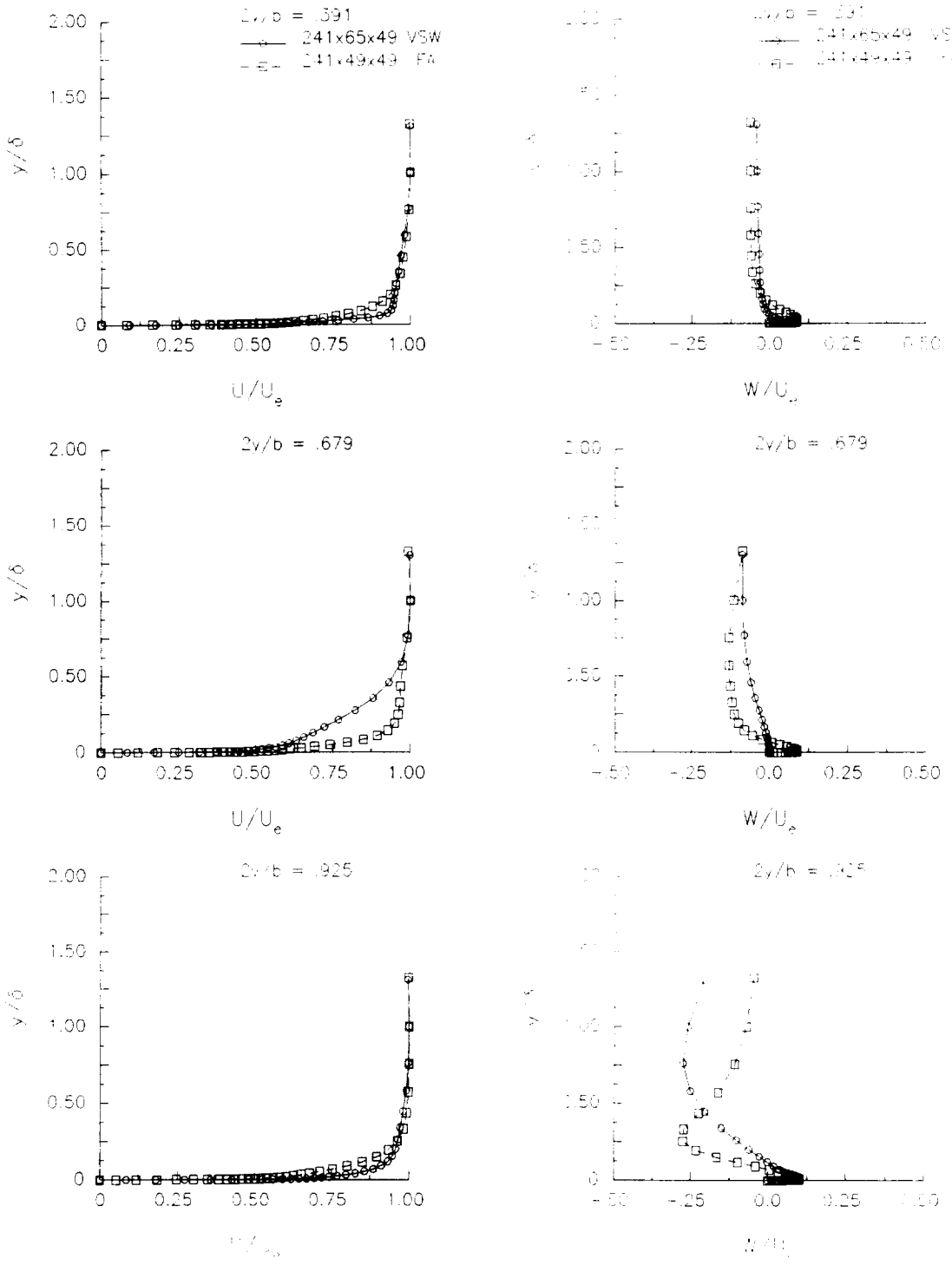

a) chordwise profiles

b) spanwise profiles

Fig. 40: Influence of sidewall boundary layer on velocity profiles for upper surface, 50%chord ($M_\infty = .8860$, $\alpha = 5.46°$, Re = medium).

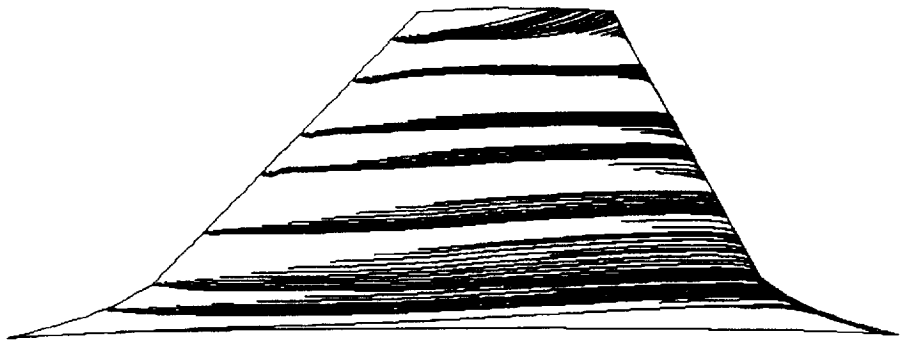

a) viscous sidewall computation

b) free-air computation

Fig. 41: Influence of sidewall boundary layer on wing streamline pattern (M_∞ = .8860, α = 5.46°, Re = medium).

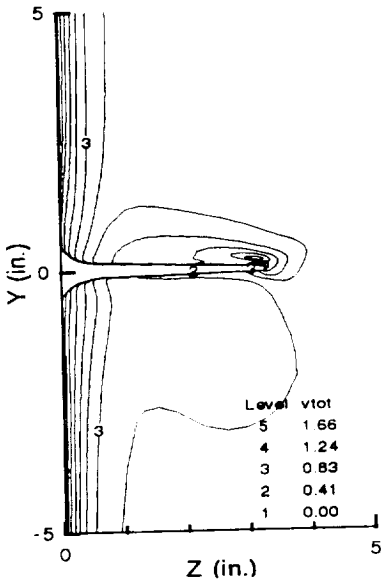

a) 25% chord

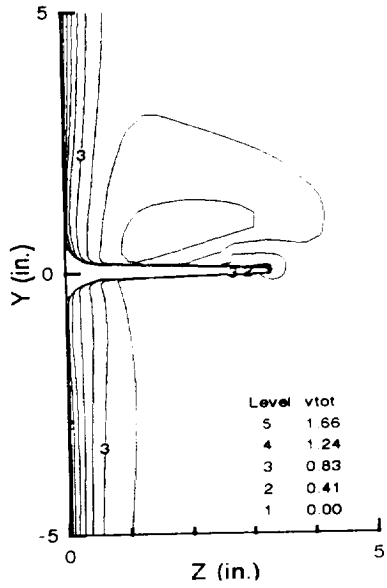

b) 50%chord

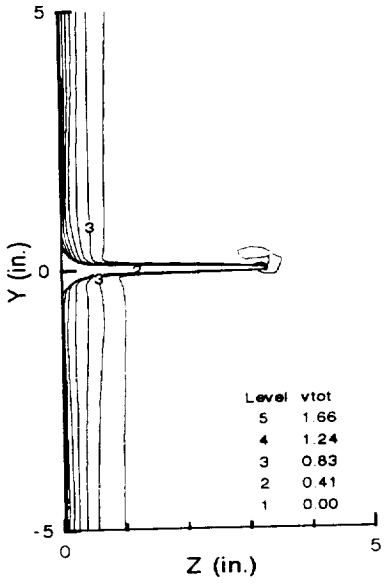

c) 75% chord

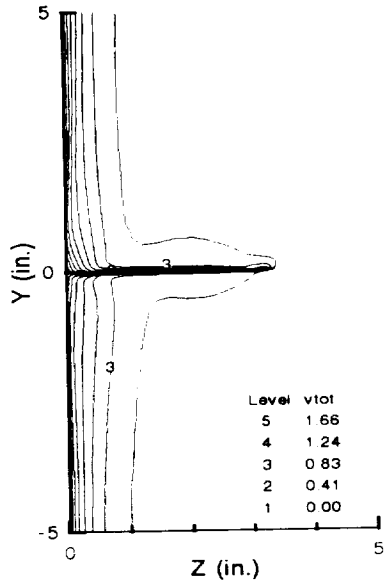

d) trailing edge

Fig. 42: Total velocity contours for viscous sidewall computation ($M_\infty = .8860$, $\alpha = 5.46°$, Re = medium).

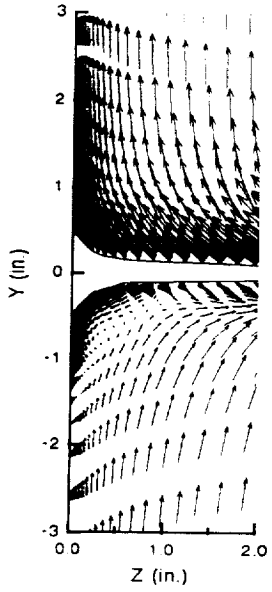

a) 25% chord

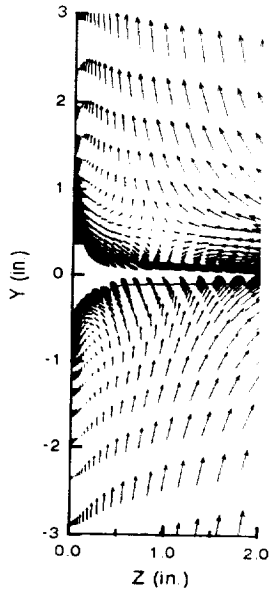

b) 50%chord

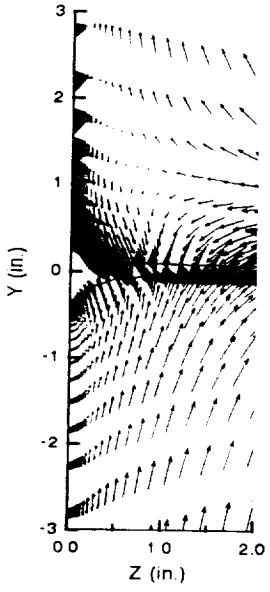

c) 75% chord

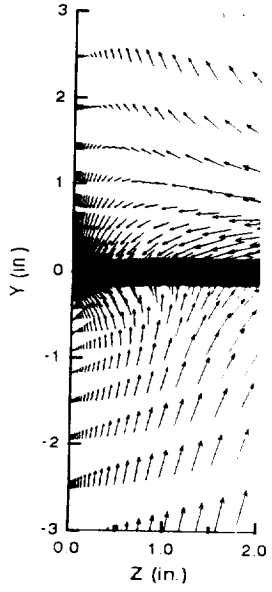

d) trailing edge

Fig. 43: Cross-flow velocity vectors, viscous sidewall computation (M_∞ = .8860. α = 5.46°. Re = medium).

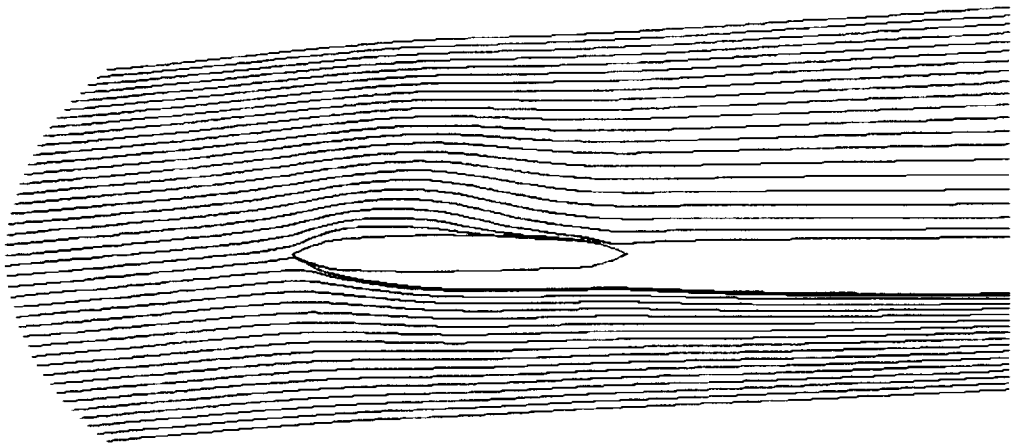

a) viscous sidewall computation

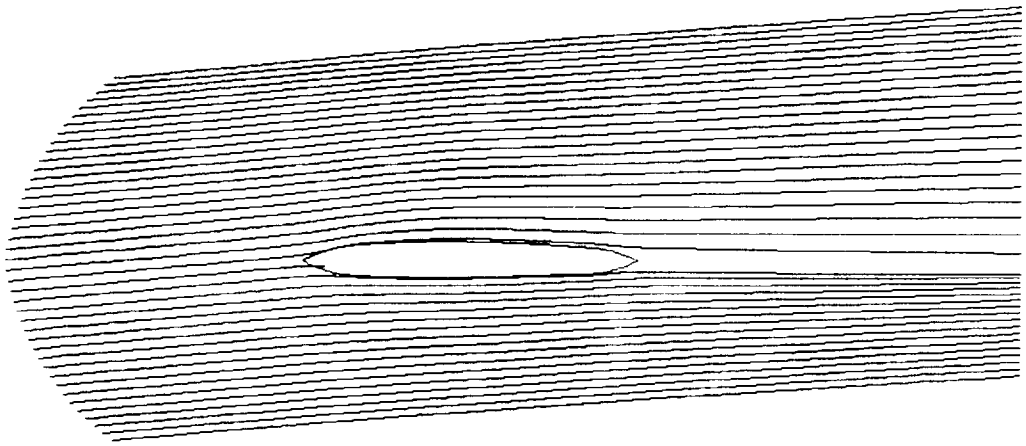

b) free-air computation

Fig. 44: Influence of sidewall boundary layer on root plane streamline pattern (M_∞ = .8860, α = 5.46°, Re = medium).

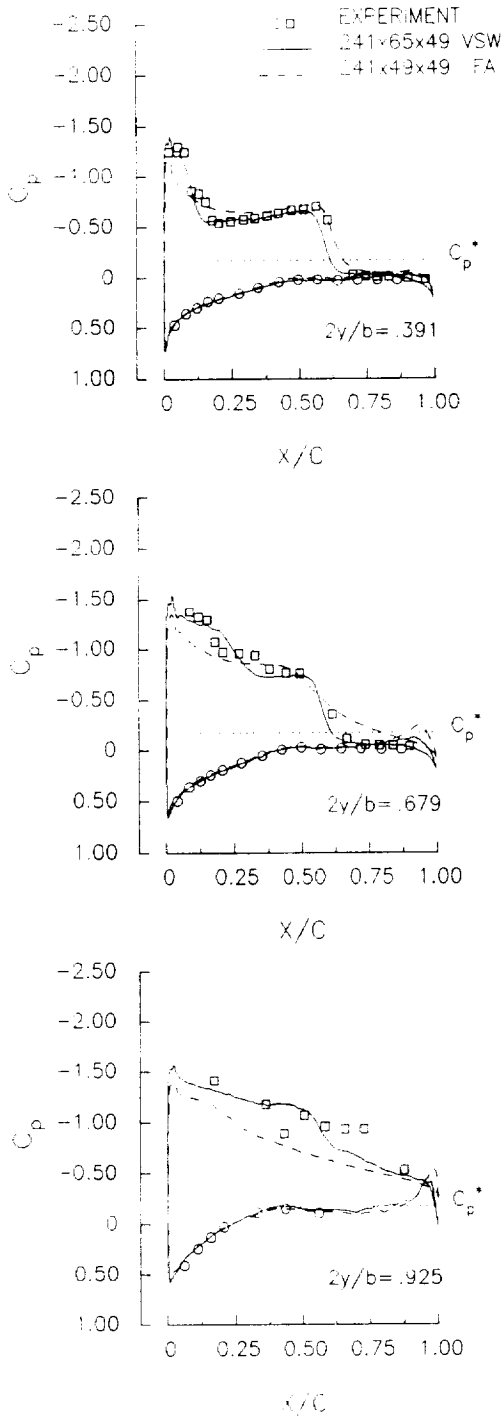

Fig. 45: Influence of sidewall boundary layer on wing surface pressure distribution ($M_\infty = .9073$, $\alpha = 10.31°$, Re = medium).

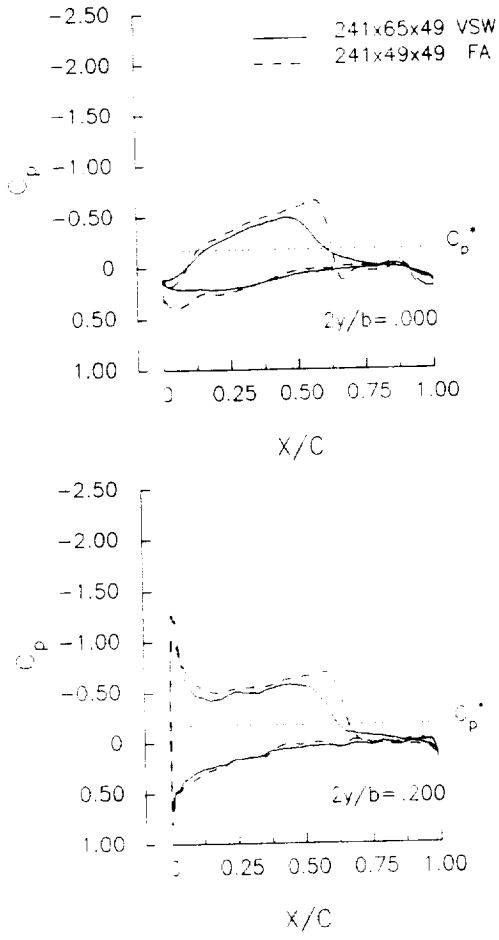

Fig. 46: Influence of sidewall boundary layer on fillet surface pressure distribution (M_∞ = .9073, α = 10.31°, Re = medium).

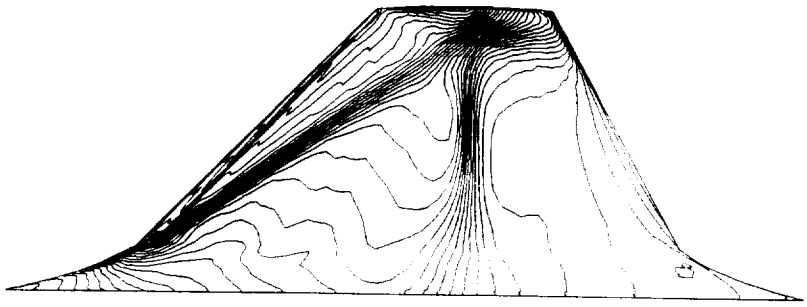

a) viscous sidewall computation

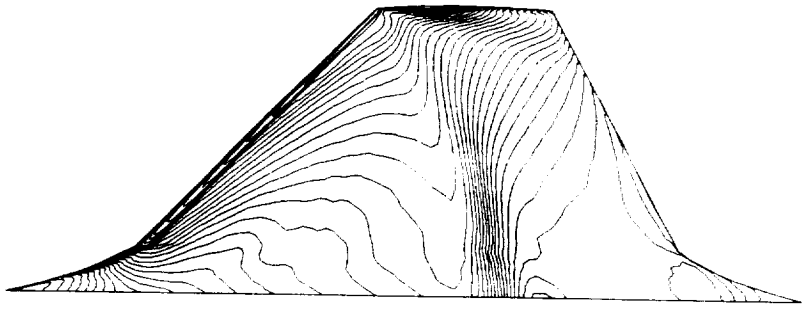

b) free-air computation

Fig. 47: Influence of sidewall boundary layer on computed surface pressure contours (M_∞ = .9073, α = 10.31°, Re = medium).

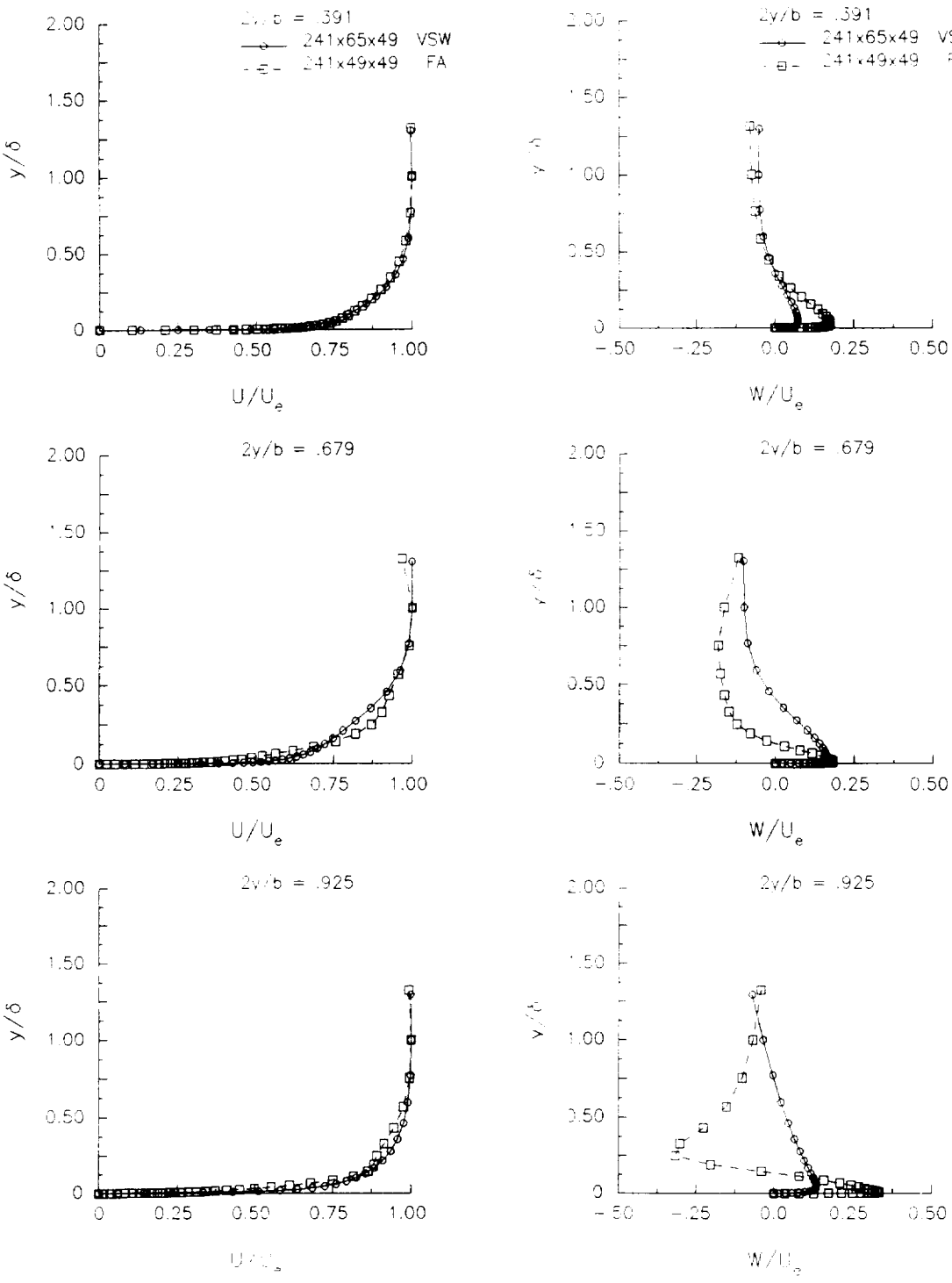

a) chordwise profiles

b) spanwise profiles

Fig. 48: Influence of sidewall boundary layer on velocity profiles for upper surface, 50%chord (M_∞ = .9073, α = 10.31°, Re = medium).

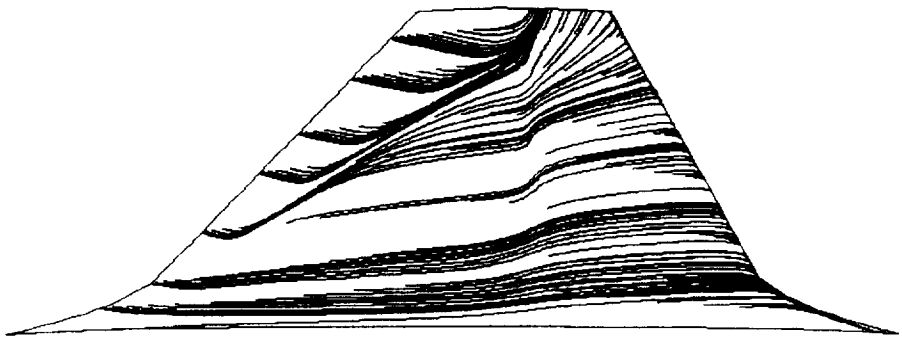

a) viscous sidewall computation

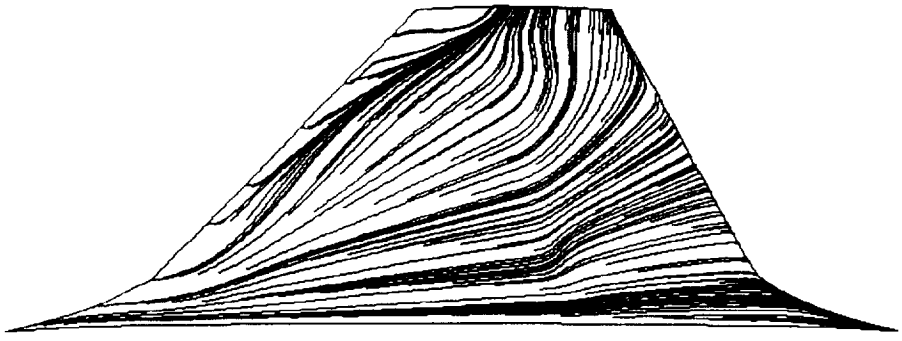

b) free-air computation

Fig. 49: Influence of sidewall boundary layer on wing streamline pattern (M_∞ = .9073, α = 10.31°, Re = medium).

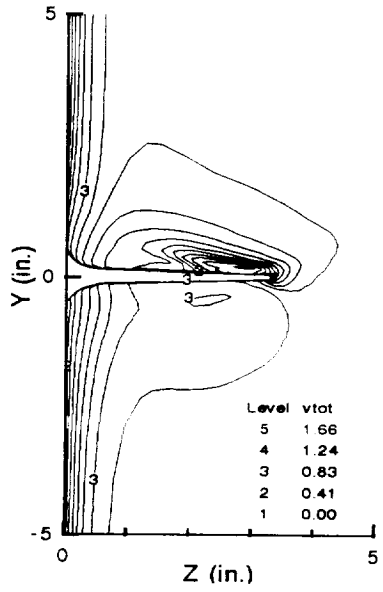

a) 25% chord

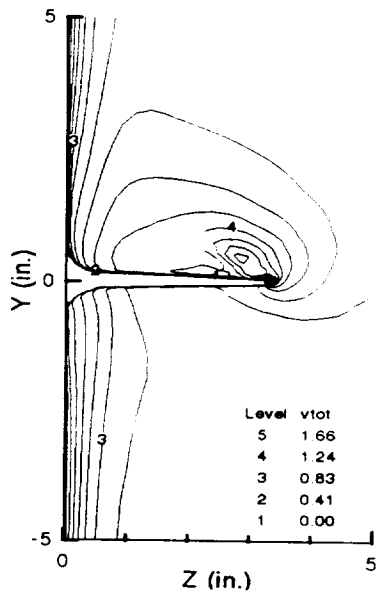

b) 50%chord

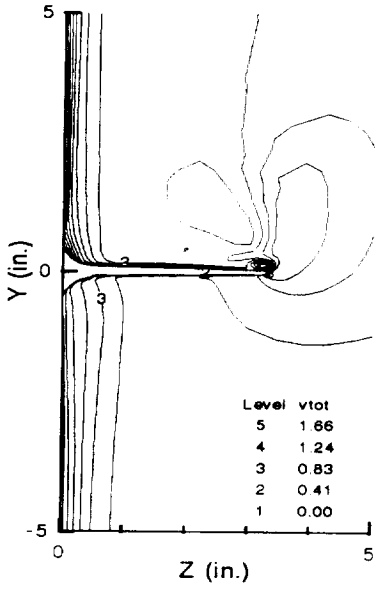

c) 75% chord

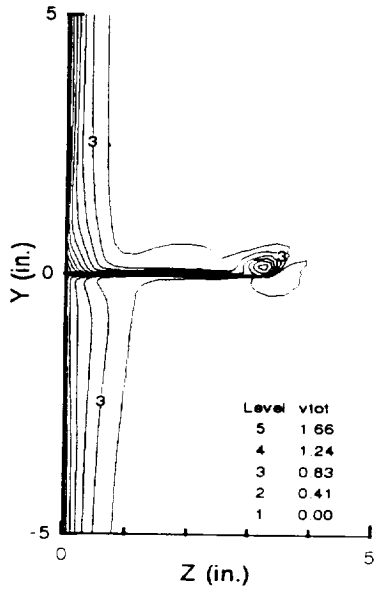

d) trailing edge

Fig. 50: Total velocity contours for viscous sidewall computation ($M_\infty = .9073$, $\alpha = 10.31°$, Re = medium).

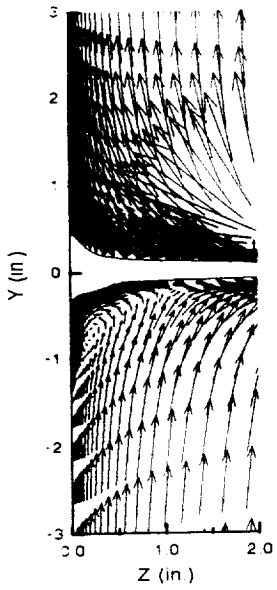

a) 25% chord

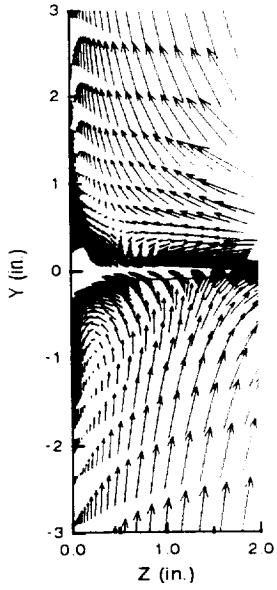

b) 50%chord

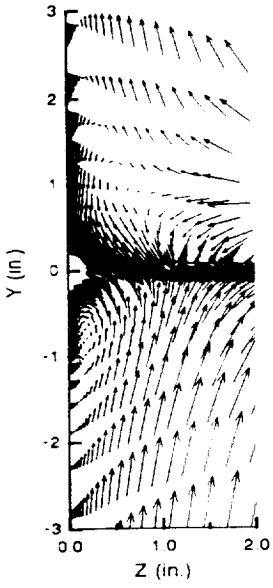

c) 75% chord

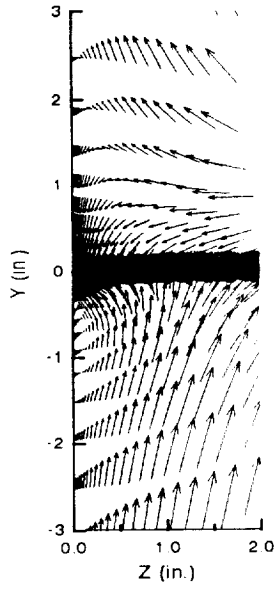

d) trailing edge

Fig. 51: Cross-flow velocity vectors, viscous sidewall computation (M_∞ = .9073, α = 10.31°, Re = medium).

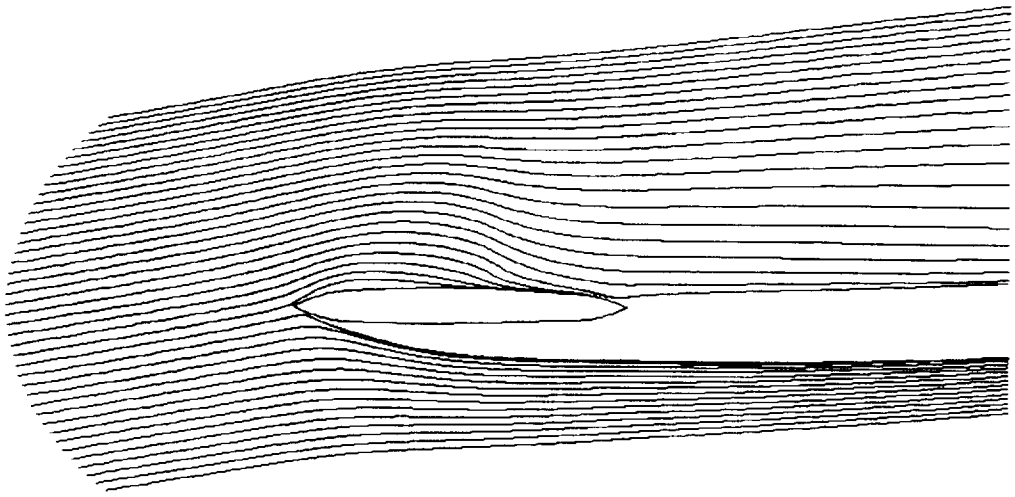

a) viscous sidewall computation

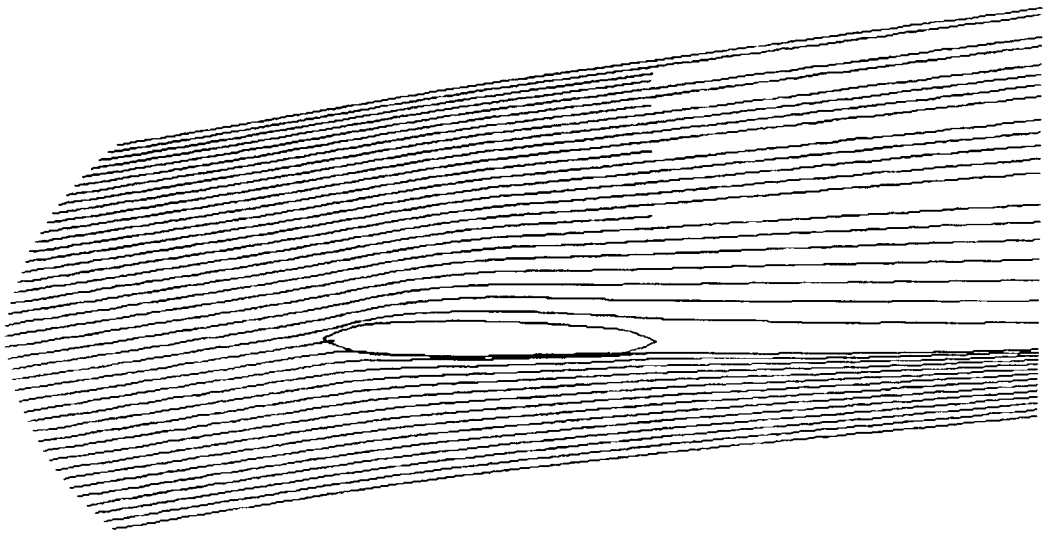

b) free-air computation

Fig. 52: Influence of sidewall boundary layer on root plane streamline pattern (M_∞ = .9073,α = 10.31°, Re = medium).